Mechanical Response of Multicrystalline Thin Films in Mesoscale Field Dislocation Mechanics

Saurabh Puri[a], Amit Das[b], Amit Acharya[b,*]

[a] Department of Mechanical Engineering, California Institute of Technology, Pasadena, CA 91125, USA.

[b] Civil and Environmental Engineering, Carnegie Mellon University, Pittsburgh, PA 15213, USA.

Abstract: A continuum model of plasticity, Phenomenological Mesoscopic Field Dislocation Mechanics (*PMFDM*), is used to study the effect of surface passivation, grain orientation, grain boundary constraints and film thickness on the mechanical response of multicrystalline thin films. The numerical experiments presented in this paper show that a surface passivation layer on thin films introduces thickness dependence of the mechanical response. However, the effect of passivation decreases in films with impenetrable grain boundaries. The orientation of individual grains of the multicrystal also has a significant effect on the mechanical response. Our results are in qualitative agreement with experimental observations. A primary contribution of this work is the implementation of a jump condition that enables the modeling of important limits of grain boundary constraints to plastic flow, independent of ad-hoc constitutive assumptions and interface conditions.

Keywords: Dislocations, Grain boundaries, Plasticity, Finite elements.

1. Introduction

Experiments on metallic thin films have been done in the recent past to study their mechanical behavior (Espinosa et al., 2004; Xiang and Vlassak, 2006). It is found that for the thin films with passivation on one or more surfaces, the stress-strain response gets harder on decreasing the thickness. In the unpassivated films, mechanical response seems to be comparatively independent of the film thickness. For thin films undergoing subsequent cycles of loading and unloading, a very strong Bauschinger effect is also observed in the passivated films in comparison to the unpassivated films. The Bauschinger effect is also size dependent, with

* Corresponding Author. Tel.: +1 412 268 4566; Fax: +1 412 268 7813.
E-mail Address: acharyaamit@cmu.edu (A. Acharya)

thinner films having a high reverse plastic strain as compared to thick films (Xiang and Vlassak, 2006). This problem was analyzed by Xiang and Vlassak (2006) using the 'isotropic' strain gradient plasticity theory of Fleck and Hutchinson (2001). They were able to model the experimentally observed size effects successfully but not the Bauschinger effect. Subsequently, Nicola et al. (2006), Shishvan et al. (2010), and Shishvan and Van der Giessen (2010) used the Discrete Dislocation (DD) technique to model the deformation of thin films and successfully predicted many of the experimentally observed features. However, DD simulations are performed at very high strain rates with grain boundaries being impenetrable to dislocations.

This paper involves the analysis of the mechanical behavior of multicrystalline thin films undergoing cycles of plane strain tension and compression using *PMFDM* (Acharya and Roy, 2006). The effects of film thickness, grain orientation, and the presence/absence of surface passivation on the response during both loading and unloading are studied. A novel feature of this work, *independent of constitutive assumptions*, is to consider the effect of different classes of grain boundary constraints to plastic flow. Our theoretical structure enables such considerations, and to our knowledge this is the first instance of such a study in the modeling of thin films. Mach et al. (2010) studied texture evolution by explicitly accounting for the partial continuity in plastic flow that arises from the unconstrained grain boundary assumption, while ignoring the effects of mesoscopic dislocation transport and elastic strain. This feature of *PMFDM* is in contrast with the so-called strain-gradient crystal plasticity theories (Gurtin, 2002; Kuroda and Tvergaard, 2008; Erturk et al., 2009) where the conditions that may be imposed on boundaries are purely a constitutive proposition without any constraints from the field equations or fundamental kinematics. We discuss this issue further at the end of this section.

PMFDM provides a framework to efficiently perform such numerical experiments at physically relevant strain rates. Weaknesses of the modeling lie in the phenomenological specification of the magnitude of the plastic strain rate and a back stress model based on the polar dislocation density tensor (the Nye tensor). We consider the latter feature as a temporary weakness in our modeling as encouraging theoretical results on the explicit form of a back stress tensor have been obtained by consideration of finite deformation mesoscale Field Dislocation Mechanics that contains a dependence of the specific entropy on the mesoscale Nye tensor based on statistical

mechanical grounds (Acharya, 2011). We note that the back stress phenomenology utilized by the strain gradient crystal plasticity theories (see Erturk et al. (2009), Svendsen and Bargmann (2010), and Bargmann et al. (2010) for a comprehensive review) involve two spatial derivatives of the plastic distortion while the one we employ here involves only one. While the performance of the strain-gradient type of *crystal* plasticity theories in modeling the experimental observations of Xiang and Vlassak (2006) have not been reported as yet, the use of these various choices (including ours) for the back-stress tensor underscores the need for more fundamental theory.

Results presented in this paper are in good *qualitative* agreement with corresponding experimental observations (Xiang and Vlassak, 2006) and an effort is made to provide a simple physical interpretation for most of them. However, there are certain interesting observations for which we are unable to provide a *simple* explanation.

Returning to the discussion of some critical aspects of the gradient crystal plasticity models vis-à-vis interface conditions arising in our theoretical structure, we note that the strain-gradient crystal plasticity models work with dislocation density/slip-rate fields related to crystal orientations in particular slip systems. In the case of multi/poly-crystal modeling such density field can have meaning only within a grain, as the physical meaning of a polar dislocation density field linked to grain orientation is necessarily different in differently oriented grains. This appears to be a serious theoretical and practical impediment. Theoretically, one has a PDE for a polar dislocation density/slip-rate type within a grain and one is now faced with the enormous task of prescribing boundary conditions for each of these types at the boundary of each grain. More fundamentally, while ad-hoc boundary conditions with dubious physical interpretation[†] have been suggested, it is not clear that there is an underlying physical principle guiding such prescription and more importantly, whether important conditions of balance (e.g. Nye tensor conservation at interfaces translating to conditions on the total plastic distortion rate) are violated or not. Practically, the number of PDEs for the model increases linearly with the number of

[†] For instance a surface condition allowing free-flow of dislocations has been suggested to be modeled by setting such polar dislocation densities to vanish at the free boundary. Simple consideration of steady flow of water in a pipe across any cross section of the pipe (including a free end) makes it clear that free flow through an interface/boundary does not require the density to vanish at such an interface/boundary.

grains in the multi/poly crystal assembly and accounting for their couplings, granted an ad-hoc choice of coupling conditions, and spatial domain identities can be an onerous task.

This paper is organized as follows: governing equations of the *PMFDM* model are briefly explained in Section 2. A jump condition at an interface for polar dislocation density in the context of *PMFDM* is developed in Acharya (2007). This jump condition allows the modeling of a variety of transmission conditions at grain boundaries and its implementation is discussed in Section 3. Setup of the thin film problem is explained in Section 4 followed by a discussion of results in Section 5. The paper ends with some concluding remarks in Section 6.

A note regarding terminology: henceforth, given a scale of resolution l, we refer to the spatial average of Nye's (1953) dislocation-density tensor over a volume l^3 around a point as the *Polar Dislocation* density tensor at that point. Nye's tensor being a tensorial quantity, the dislocations that are averaged out in this process due to cancellation in sign form a density that we refer to as the *Statistically Distributed Dislocation* (SD) density. Thus, the difference of local value of Nye's tensor field and its spatial average is referred to as SD.

2. Theory

A theory of fine-scale dislocation mechanics, Field Dislocation Mechanics (*FDM*), has been proposed in Acharya (2001, 2003), building on the pioneering works of Kroner (1981), Mura (1963), and Willis (1967). The Phenomenological Mesoscopic Field Dislocation Mechanics (*PMFDM*) model (Acharya and Roy, 2006) is obtained by an elementary space-time averaging of the equations of *FDM* using a standard procedure utilized in the study of multiphase flows (e.g. Babic, 1997). The governing equations of *PMFDM* are summarized in this section. The (symmetric) stress tensor $\boldsymbol{T}$ satisfies

$$\begin{aligned} \boldsymbol{T} &= \boldsymbol{C} : \boldsymbol{U}^e \\ div\boldsymbol{T} &= \boldsymbol{0} \end{aligned} \tag{1}$$

along with standard traction/displacement boundary conditions. $\boldsymbol{C}$ is the possibly anisotropic fourth order tensor of linear elastic moduli and $\boldsymbol{U}^e$ is the elastic distortion tensor defined as

$$\boldsymbol{U}^e = grad\ \boldsymbol{u} - \boldsymbol{U}^p. \tag{2}$$

In the above equation, $\boldsymbol{u}$ is the total displacement field and $\boldsymbol{U}^p$ is the plastic distortion tensor which is decomposed uniquely into compatible and incompatible parts as

$$\boldsymbol{U}^p = grad\,\boldsymbol{z} - \boldsymbol{\chi}, \tag{3}$$

where $\boldsymbol{z}$ is the plastic displacement and $\boldsymbol{\chi}$ is the incompatible part of the elastic distortion.

Thus, the elastic distortion tensor may be rewritten as,

$$\boldsymbol{U}^e = grad(\boldsymbol{u} - \boldsymbol{z}) + \boldsymbol{\chi}, \tag{4}$$

where the field $\boldsymbol{\chi}$ cannot be written as a non-trivial gradient. The incompatible part, $\boldsymbol{\chi}$, is given by

$$\begin{aligned} curl\,\boldsymbol{\chi} &= \boldsymbol{\alpha} \\ div\,\boldsymbol{\chi} &= \boldsymbol{0} \end{aligned} \tag{5}$$

where $\boldsymbol{\alpha}$ is space-time averaged polar dislocation density tensor field. The vector field $\boldsymbol{z}$ whose gradient represents the compatible part of $\boldsymbol{U}^p$ obeys the relation

$$div\left(grad\,\dot{\boldsymbol{z}}\right) = div\left(\boldsymbol{\alpha}\times\boldsymbol{V} + \boldsymbol{L}^p\right) \tag{6}$$

where $\boldsymbol{V}$ is the averaged polar dislocation velocity vector, and $\boldsymbol{L}^p$ represents that part of the total slip strain rate which is not represented by the slipping produced by the polar dislocation density. Finally the temporal evolution of the polar dislocation density tensor field is prescribed as

$$\begin{aligned} \dot{\boldsymbol{\alpha}} &= -curl\ \boldsymbol{S} + \boldsymbol{s} \\ \boldsymbol{S} &:= \boldsymbol{\alpha}\times\boldsymbol{V} + \boldsymbol{L}^p, \end{aligned} \tag{7}$$

where $\boldsymbol{S}$ is the averaged slipping distortion (slip rate), and $\boldsymbol{s}$ is the nucleation rate field. Since $\boldsymbol{\alpha}$ is a solenoidal field, i.e. divergence free, $\boldsymbol{s}$ can be written as a curl of a second order tensor valued nucleation rate potential field, $\boldsymbol{\Omega}$:

$$\boldsymbol{s} = curl\ \boldsymbol{\Omega}. \tag{8}$$

2.1 Boundary Conditions

The following boundary conditions are admitted:

a. $\boldsymbol{\chi}\boldsymbol{n} = \boldsymbol{0}$ on the boundary ∂B of the body with outward unit normal $\boldsymbol{n}$.

b. $\left(grad\,\dot{\boldsymbol{z}}\right)\boldsymbol{n} = \left(\boldsymbol{\alpha}\times\boldsymbol{V} + \boldsymbol{L}^p\right)\boldsymbol{n}$ *on* ∂B.

c. Standard displacement/traction boundary conditions on ∂B.

d. Equation $(7)_1$ admits boundary conditions on the dislocation flow (Acharya and Roy, 2006). In general, a natural boundary condition of the form

$$\boldsymbol{S}\times\boldsymbol{n}=\boldsymbol{\Phi} \tag{9}$$

where $\boldsymbol{\Phi}$ is a (second-order tensor-valued) specified function of time and position along the boundary satisfying the constraint $\boldsymbol{\Phi n}=\boldsymbol{0}$ is appropriate to model controlled flow at the boundary. A rigid boundary with respect to slipping may be represented with a zero flow boundary condition

$$\boldsymbol{S}\times\boldsymbol{n}=\boldsymbol{0} \tag{10}$$

on the entire boundary. Imposing such a boundary condition can lead to the development of shocks or discontinuities. A less restrictive boundary condition is the imposition of the dislocation flux, $\boldsymbol{\alpha}\left(\boldsymbol{V}\cdot\boldsymbol{n}\right)$, on inflow points of the boundary (where $\boldsymbol{V}\cdot\boldsymbol{n}<0$) along with a specification of $\boldsymbol{L}^p\times\boldsymbol{n}$ on the entire boundary. This condition allows free exit of polar dislocations without any added specification.

2.2 Initial Conditions

The initial conditions on the fields $\boldsymbol{u}$, $\boldsymbol{\alpha}$ and $grad\,\boldsymbol{z}$ are as follows. For the $\boldsymbol{u}$ field we assume $\boldsymbol{u}\big|_{t=0}\equiv\boldsymbol{0}$, which is a physically natural initial condition on the displacement field. Unless otherwise mentioned, we assume that the body is initially polar dislocation free which translates to $\boldsymbol{\alpha}\big|_{t=0}=\boldsymbol{0}$. The initial condition on the $grad\,\boldsymbol{z}$ field is obtained from solving (5) and (1), with $\boldsymbol{u}\big|_{t=0}=\boldsymbol{0}$.

2.3 Auxiliary Condition

The value of $\dot{\boldsymbol{z}}$ is prescribed at an arbitrarily chosen point of the body and in our case is assumed to vanish without loss of generality.

2.4 Constitutive Specifications

Physically reasonable choices for $\boldsymbol{V}$ and $\boldsymbol{L}^p$ are made based on the requirement of non-negativity of plastic working, pressure-independence of plastic flow and ingredients of conventional crystal plasticity theory. They are mentioned below.

$$\begin{aligned} \boldsymbol{L}^p &= sym\left(\sum_{\kappa=1}^{n_{slip}} \dot{\gamma}^{\kappa} \boldsymbol{m}_0^{\kappa} \otimes \boldsymbol{n}_0^{\kappa}\right) \\ \boldsymbol{V} &= v\frac{\boldsymbol{d}}{|\boldsymbol{d}|} \;\; ; \;\; v \geq 0 \end{aligned} \tag{11}$$

where $sym(\bullet)$ implies the symmetric part of $(\bullet)$, n_{slip} is the total number of slip systems, $\boldsymbol{m}_0^{\kappa}$ and $\boldsymbol{n}_0^{\kappa}$ are the unstretched unit slip direction and normal, respectively, $\boldsymbol{d}$ is the direction of the polar dislocation velocity, $\dot{\gamma}^{\kappa}$ represents the magnitudes of SD slipping rate on the slip system κ and v is the averaged velocity of polar dislocations. A power law is used for $\dot{\gamma}^{\kappa}$

$$\dot{\gamma}^{\kappa} = \dot{\gamma}_0^{\kappa} sgn(\tau^{\kappa} - \Omega^{\kappa}) \left(\frac{\left|\tau^{\kappa} - \Omega^{\kappa}\right|}{g}\right)^{\frac{1}{m}} \tag{12}$$

where τ^{κ} is the resolved shear stress on slip system κ, Ω^{κ} (scalar for each κ) is the back stress corresponding to the individual slip system κ, m is the rate-sensitivity of the material, g is the strength of the material, and $\dot{\gamma}_0^{\kappa}$ is a reference strain rate on the slip system κ. The expression of back stress evolution is based on the Armstrong–Frederick (1966) form as in Harder (1999) but is a function of polar dislocation density (cf. Taupin et al., 2007):

$$\dot{\Omega}^{\kappa} = \left(\left|\alpha \boldsymbol{m}_0^{\kappa}\right| + \left|\alpha \boldsymbol{p}_0^{\kappa}\right|\right) L\mu\dot{\gamma}^{\kappa} - c\Omega^{\kappa}\left|\dot{\gamma}^{\kappa}\right|; \boldsymbol{p}_0^{\kappa} = \boldsymbol{m}_0^{\kappa} \times \boldsymbol{n}_0^{\kappa} \tag{13}$$

where L is the hardening coefficient and c is the recovery coefficient. The back stress evolves only if there is a non-zero polar dislocation content in the body. The space-time averaged polar dislocation density tensor is not capable of transmitting information on the spatial concentrations of microscopic dislocation density to the calculation of stress in *PMFDM*. For the structural thin film length scales involved, these concentrations can be important and thus have to be modeled. The form of such a model fundamentally rests on the accurate spatio-temporal coarse graining of the very nonlinear underlying set of equations representing the motion of individual dislocations,

represented either discretely or by PDE – an as yet unsolved, formidable theoretical challenge. Here, we make incremental progress relying on simple, established back-stress phenomenology adapted to our case through the dependence on the polar dislocation density.

The resolved shear stress τ^{κ} is calculated as follows:

$$\tau^{\kappa} = \boldsymbol{m}_0^{\kappa} \cdot \boldsymbol{T}\boldsymbol{n}_0^{\kappa} \tag{14}$$

The direction of polar dislocation velocity $\boldsymbol{d}$ is

$$\begin{aligned} &\boldsymbol{d} \coloneqq \boldsymbol{f} - \left(\boldsymbol{f} \cdot \frac{\boldsymbol{a}}{|\boldsymbol{a}|} \right) \frac{\boldsymbol{a}}{|\boldsymbol{a}|}, \\ &\boldsymbol{f} \coloneqq \boldsymbol{X}\left(\boldsymbol{T}'\boldsymbol{\alpha}\right) \;;\; f_i = e_{ijk} T'_{jr} \alpha_{rk} \quad ; \quad \boldsymbol{a} \coloneqq \boldsymbol{X}\left(tr\left(\boldsymbol{T}\right)\boldsymbol{\alpha}\right) \;;\; a_i = \left(\frac{1}{3} T_{mm}\right) e_{ijk} \alpha_{jk}. \end{aligned} \tag{15}$$

The definition of the direction $\boldsymbol{d}$ can be approached from two points of view. In the situation when the polar dislocation density may not be expressed as an elementary dyad formed from a Burgers vector direction and a line direction, the definition arises as a sufficient condition for pressure independence of the polar dislocation plastic strain rate and ensuring positive dissipation. The dissipation in the model can be written as

$$D = \int_B \left(\boldsymbol{X}\left(\boldsymbol{T}\boldsymbol{\alpha}\right) \cdot \boldsymbol{V} + \boldsymbol{T} : \boldsymbol{L}^p \right) dv \,. \tag{16}$$

Focusing on the dissipation due to polar dislocation motion, $\boldsymbol{X}\left(\boldsymbol{T}\boldsymbol{\alpha}\right) \cdot \boldsymbol{V}$, and writing

$$\boldsymbol{X}\left(\boldsymbol{T}\boldsymbol{\alpha}\right) = \boldsymbol{f} + \boldsymbol{a} \tag{17}$$

where $\boldsymbol{f}$ is a pressure-independent term, it makes physical sense to require $\boldsymbol{V}$ to be in the direction of $\boldsymbol{f}$. However, this does not guarantee that the dissipation due to polar dislocation motion is independent of pressure and neither that $\boldsymbol{X}\left(\boldsymbol{T}\boldsymbol{\alpha}\right) \cdot \boldsymbol{f} \geq \boldsymbol{0}$; however subtracting the component of $\boldsymbol{f}$ in the direction of $\boldsymbol{a}$ ensures the latter fact:

$$\left(\boldsymbol{f} + \boldsymbol{a}\right) \cdot \left(\boldsymbol{f} - \left(\boldsymbol{f} \cdot \frac{\boldsymbol{a}}{|\boldsymbol{a}|} \right) \frac{\boldsymbol{a}}{|\boldsymbol{a}|} \right) = \boldsymbol{f} \cdot \boldsymbol{f} - \frac{\left(\boldsymbol{f} \cdot \boldsymbol{a}\right)^2}{|\boldsymbol{a}|^2} + \boldsymbol{a} \cdot \boldsymbol{f} - \boldsymbol{f} \cdot \boldsymbol{a} = \boldsymbol{f} \cdot \boldsymbol{f} - \left(\boldsymbol{f} \cdot \frac{\boldsymbol{a}}{|\boldsymbol{a}|} \right)^2 \geq 0 \tag{18}$$

by Pythagoras' theorem.

Alternatively, a compelling mechanistic interpretation arises when $\boldsymbol{\alpha}$ may be interpreted as an elementary dyad formed from a Burgers vector direction and a line direction, say $\boldsymbol{b} \otimes \boldsymbol{l}$. Then the

direction of $\boldsymbol{a}$ represents the direction of climb whenever $\boldsymbol{\alpha}$ represents a dislocation segment of pure edge or mixed character (and it is degenerate when $\boldsymbol{\alpha}$ is of pure screw character); thus $\boldsymbol{d}$ represents the fact that mixed or edge dislocations cannot climb whereas screw dislocations are unrestricted in their motion.

The expression for v is assumed to be

$$v(state) = \frac{\eta^2 b}{n_{slip}} \left(\frac{\mu}{g} \right)^2 \sum_{\kappa=1}^{n_{slip}} \dot{\gamma}^{\kappa} \tag{19}$$

where μ is the shear modulus, b the Burgers vector magnitude and $\eta = 1/3$ a material parameter. The strength of the material is assumed to evolve according to

$$\dot{g} = \left[\frac{\eta^2 \mu^2 b}{2(g - g_0)} k_0 \left| \boldsymbol{\alpha} \boldsymbol{n}_0^{\kappa} \right| + \theta_0 \left(\frac{g_s - g}{g_s - g_0} \right) \right] \left\{ \left| \boldsymbol{\alpha} \times \boldsymbol{V} \right| + \sum_{\kappa=1}^{n_{slip}} \dot{\gamma}^{\kappa} \right\} \tag{20}$$

where g_s is the saturation stress, g_0 is the yield stress, and θ_0 is the Stage II hardening rate. k_0 is an extra parameter in the *PMFDM* model that needs to be fitted experimentally. The details of the numerical implementation of the equations using the Finite Element Method is described in Roy and Acharya (2005), Roy and Acharya (2006), Puri et al. (2010) and Puri (2009).

3. Jump Condition for Polar Dislocation Density

The jump condition for polar dislocation density along a *material* interface in *PMFDM* (Acharya, 2007) is summarized in this section. At a *material interface* it reduces to

$$[\![\boldsymbol{S}]\!] \times \boldsymbol{n} + [\![\boldsymbol{\eta}]\!] \times \boldsymbol{n} = \boldsymbol{0} . \tag{21}$$

where $[\![(\bullet)]\!]$ represents a jump in $(\bullet)$ across the interface. The value of $\boldsymbol{\eta}$ can be set in accord with the nature of the grain boundary; in this paper the grain boundary is assumed not to be a source/sink. This corresponds to $[\![\boldsymbol{\eta}]\!] = \boldsymbol{0}$. Thus, (21) reduces to

$$[\![\boldsymbol{S}]\!] \times \boldsymbol{n} = \boldsymbol{0} . \tag{22}$$

Physically, (22) embodies the simple fact that in the absence of sources and sinks on any surface in the body, the plastic distortion rate arising due to the motion of all dislocations (both polar dislocations and SD) on a given side of the surface has to match the same quantity on the other side. The condition (22), with a restricted definition of $\boldsymbol{S}$ than used here, was proposed in Gurtin and Needleman (2005). However, there it is an extraneous assumption, whereas in our model this is a fundamental statement of balance at an interface, independent of constitutive specification. We note here that (22) is a special case of a jump condition at a non-material interface (Acharya, 2007) that, in general, moves with respect to the material.

Consider a sample consisting of two grains, B_1 and B_2, with c being the interface between them; $\boldsymbol{n}$ is a unit normal to the interface (as shown in Figure 1(a)). For this idealized problem, (22) can be written as

$$\left(\boldsymbol{S}_1 - \boldsymbol{S}_2\right) \times \boldsymbol{n} = \boldsymbol{0}\,, \tag{23}$$

where $\boldsymbol{S}_1$ and $\boldsymbol{S}_2$ correspond to grains $\boldsymbol{B}_1$ and $\boldsymbol{B}_2$, respectively. This jump condition can be satisfied in two ways:

a. Imposing $\left(\boldsymbol{S}_1 - \boldsymbol{S}_2\right) \times \boldsymbol{n} = \boldsymbol{0}$ on the interface, c.

b. Imposing $\boldsymbol{S}_1 \times \boldsymbol{n} = \boldsymbol{0}$ and $\boldsymbol{S}_2 \times \boldsymbol{n} = \boldsymbol{0}$ on the interface, c.

Case (a) allows free flow of dislocations across a grain boundary. Case (b) allows the modeling of completely constrained (blocked) plastic flow on either side of the grain boundary. This corresponds to the idealized situation of the grain boundary being impenetrable to dislocations.

3.1 Numerical Implementation of the Jump Condition

Now we discuss the imposition of conditions (a) and (b) mentioned in Section 3 in the finite element framework for the sample with grains B_1 and B_2 (Figure 1(a)). The weak formulation of $(7)_1$ for the two grains can be written as

$$\begin{aligned} \int_{B_1} \dot{\boldsymbol{\alpha}} : \delta\boldsymbol{\alpha}\; dv &= -\int_{B_1} \boldsymbol{S} : curl\left(\delta\boldsymbol{\alpha}\right)\; dv + \int_{B_1} \boldsymbol{\eta} : curl\left(\delta\boldsymbol{\alpha}\right)\; dv \\ \int_{B_2} \dot{\boldsymbol{\alpha}} : \delta\boldsymbol{\alpha}\; dv &= -\int_{B_2} \boldsymbol{S} : curl\left(\delta\boldsymbol{\alpha}\right)\; dv + \int_{B_2} \boldsymbol{\eta} : curl\left(\delta\boldsymbol{\alpha}\right)\; dv, \end{aligned} \tag{24}$$

where the symbol $\delta\boldsymbol{\alpha}$ represents a test function.

Integrating (24) by parts and choosing a sufficiently piece-wise smooth $\delta\boldsymbol{\alpha}$ such that its value is non-zero along a thin (3-d) sliver along the grain boundary and is zero everywhere else, (24) reduces to

$$\begin{aligned}\int_{c_{B_1}} \left(\boldsymbol{S}_1 \times \boldsymbol{n}\right) : \delta\boldsymbol{\alpha}_1 \, da + \int_{c_{B_2}} \left(\boldsymbol{S}_2 \times \boldsymbol{n}\right) : \delta\boldsymbol{\alpha}_2 \, da = \\ \int_{c_{B_1}} \left(\boldsymbol{\eta}_1 \times \boldsymbol{n}\right) : \delta\boldsymbol{\alpha}_1 \, da + \int_{c_{B_2}} \left(\boldsymbol{\eta}_2 \times \boldsymbol{n}\right) : \delta\boldsymbol{\alpha}_2 \, da + E_{gb},\end{aligned} \tag{25}$$

where E_{gb} is a term that can be made arbitrarily small by choosing the width of the sliver and $\delta\boldsymbol{\alpha}_i, i = 1,2$ are the values of the piecewise smooth test function on the grain boundary. Since $\boldsymbol{\eta_1} = \boldsymbol{\eta_2} = \boldsymbol{0}$ and $\boldsymbol{n_1} = -\boldsymbol{n_2} = \boldsymbol{n}$, when the test function is assumed to be continuous on the bi-crystal, (25) implies

$$\int_c \left(\left(\boldsymbol{S_1} - \boldsymbol{S_2}\right) \times \boldsymbol{n}\right) : \delta\boldsymbol{\alpha} \; da = 0 \quad \Rightarrow \quad \left(\boldsymbol{S_1} - \boldsymbol{S_2}\right) \times \boldsymbol{n} = \boldsymbol{0} \quad \text{on } c.. \tag{26}$$

This corresponds to the implementation of case (a) mentioned in Section 3. The plastic flow at the grain boundary cannot be stopped by imposing this condition. However, the formulation also allows the use of discontinuous, piece-wise smooth test functions. In such a case,(25) implies

$$\int_c \left(\boldsymbol{S}_1 \times \boldsymbol{n}\right) : \delta\boldsymbol{\alpha}_1 \, da - \int_c \left(\boldsymbol{S}_2 \times \boldsymbol{n}\right) : \delta\boldsymbol{\alpha}_2 \, da = 0, \tag{27}$$

and since $\delta\boldsymbol{\alpha}_1$ and $\delta\boldsymbol{\alpha}_2$ can be chosen arbitrarily and independently of each other, (27) allows us to impose the conditions, $\boldsymbol{S}_1 \times \boldsymbol{n} = \boldsymbol{0}$ and $\boldsymbol{S}_2 \times \boldsymbol{n} = \boldsymbol{0}$ on c in the respective grains. This corresponds to the implementation of case (b) mentioned in Section 3.

In order to model (27) in the finite element framework, two node numbers are assigned to each node of the grain boundary as shown in Figure 1(b). All the nodes of the grain boundary are characterized as surface nodes. The following fields are set to be equal on the two nodes using linear multipoint constraints:

$$\begin{aligned} \boldsymbol{u}\big|_2 &= \boldsymbol{u}\big|_3 & \qquad \boldsymbol{u}\big|_6 &= \boldsymbol{u}\big|_7 \\ \boldsymbol{z}\big|_2 &= \boldsymbol{z}\big|_3 & \qquad \boldsymbol{z}\big|_6 &= \boldsymbol{z}\big|_7 \\ \boldsymbol{\chi}\big|_2 &= \boldsymbol{\chi}\big|_3 & \qquad \boldsymbol{\chi}\big|_6 &= \boldsymbol{\chi}\big|_7 . \end{aligned} \tag{28}$$

where $(\bullet)\big|_i$ represents the value of the field $(\bullet)$ at node i. The conditions (28) with $\boldsymbol{S}_1 \times \boldsymbol{n} = \boldsymbol{0}$ and $\boldsymbol{S}_2 \times \boldsymbol{n} = \boldsymbol{0}$ on the interface c correspond to the constrained plastic flow case. In the finite element setting, the constraints (28) imply that test functions corresponding to these fields are continuous on the grain boundary. Thus, if in addition $\boldsymbol{\alpha}\big|_2 = \boldsymbol{\alpha}\big|_3$ is also considered, the unconstrained plastic flow situation corresponding to the 'single-noded' grain boundary case is recovered. This provides an independent check for the 'double-noded' grain boundary simulations.

4. Problem Setup

For all the simulations mentioned in this chapter, a multicrystal consisting of four grains as shown in Figure 2 is used. Samples are unstressed and polar dislocations free initially. The dimensions of thin films used in the computations presented in this paper are motivated from the experiments done by Xiang and Vlassak (2006). Each grain has a thickness h and width w. Two different values of h are used, $h = 0.35\mu m$ and $h = 1.4\mu m$ and w is set to be equal to $0.33\mu m$. c_s shown in Figure 2 is equal to $0.5\mu m$. Two cases, (a) with passivation layer on both surfaces, and (b) with no surface passivation, are considered. Furthermore, three different sets of orientation of grains in the multicrystal are considered:

1. Misorientation between adjacent grains is 3-5 degrees about the x_3-axis. The Bunge Euler angles (in degrees) for the four grains on going from left to right in Figure 2 are (2,0,0), (0,0,0), (5,0,0), (3,0,0).
2. Misorientation between adjacent grains is 20-30 degrees about the x_3-axis. The Bunge Euler angles (in degrees) for the four grains on going from left to right in Figure 2 are (25,0,0), (0,0,0), (45,0,0), (30,0,0).
3. In the third case, orientation of the 12 slip systems of a cubic crystal is changed such that a (111) plane is parallel to the $x_1 - x_3$ plane. Now, the grains are rotated about the x_2-axis such that misorientation between adjacent grains is 3-5 degrees. Specifically, grain 1 is rotated

anticlockwise by 3 degrees, grain 2 by 0 degrees, grain 3 by 5 degrees and grain 4 by 2 degrees.

Material parameters representative of Copper are used for all the computational experiments presented in this chapter; $b = 2.5\times10^{-4}\,\mu$m, $m = 0.03$, $g_s = 210$ MPa, $g_0 = 50$ MPa, $\theta_0 = 205$ MPa, $k_0 = 20.0$, $n_{slip} = 12$, $L = 100$, and $c = 100$. The physical meaning of these parameters is described in Section 2. The reference strain rate is $\dot{\gamma}_0 = 1\,\text{sec}^{-1}$. Isotropic elastic constants of the representative material are $E = 110$ GPa, $\upsilon = 0.34$, where E is the Young's modulus and υ is the Poisson's ratio. The *passivation layer(s) is considered as elastic* with elastic constants representing Silica with $E = 70$GPa, and $\upsilon = 0.17$. The thickness of the passivation layer is set to $0.02\mu m$ in all computations.

The imposed initial conditions are mentioned in Section 2. The displacement boundary conditions corresponding to plain strain tension are applied in the following way (Figure 2):

$u_1 = 0$ at $x_1 = 0$

$u_2 = 0$ at $x_2 = 0$

$u_3 = 0$ at $x_3 = c_s$

$u_1 = (4w)\dot{\varepsilon}t$ at $x_1 = 4w$

where $\dot{\varepsilon}$ is an applied tensile strain rate of 1 sec^{-1}, and t is time. The left and the right faces are traction free in the x_2, x_3 directions. The bottom face is traction free in the x_1, x_3 directions and the top face is traction free in the x_1, x_2, x_3 directions. The front face is traction free in the x_1, x_2 directions. In order to do a two dimensional problem in the current setup, all degrees of freedom on the back face are set to be equal to the value of corresponding degrees of freedom on the front face. The boundary conditions for imposing constrained/unconstrained plastic flow through the grain boundaries are mentioned in Section 3. All components of the polar dislocation density ($\boldsymbol{\alpha}$) on the left external face are set to be equal to the components of corresponding nodes on the right face. This implies that the dislocation flow on the right face is equal and opposite to that on the left face.

$$\boldsymbol{\alpha}\big|_L = \boldsymbol{\alpha}\big|_R \tag{29}$$

In the interpretation of results, the contribution of passivation layers is removed from the flow stress by plotting the volume average of 11 component of stress $\boldsymbol{T}$ over the elastic-plastic elements only against the applied strain ε . $\langle \boldsymbol{T}_{11} \rangle$ is denoted by σ in the plots and rest of the text.

A mesh refinement study is done in order to choose an optimum mesh for computations. A film of thickness $0.35\mu m$ with a surface passivation layer on both sides is considered for this purpose. The grain boundaries are assumed to be impenetrable to plastic flow. The average stress-strain response for meshes of different sizes is shown in Figure 3(a). Mesh dimension in the legend of Figure 3(a) represents the discretization of the film in $x_1, x_2,$ and x_3 direction (eg. 16 x 14 x 1 implies 16 elements in x_1 direction, 14 elements in x_2 direction and 1 element in x_3 direction). Average stress seems to increase with mesh refinement. An upper bound to the stress at 1% applied strain is estimated using extrapolation as shown in Figure 3(b). Figure 3(c) indicates refinement of the spatial pattern of $|\boldsymbol{\alpha}|$ on decreasing the element size (however, the magnitude of $|\boldsymbol{\alpha}|$ appears to be increasing with mesh refinement). The element size corresponding to the mesh with dimensions 16 x 14 x 1 seems to be a conservative choice although the average stress at 1% applied strain for this mesh size is lesser than the linearly extrapolated stress for zero element size by 4%. All the simulations presented in this paper (regardless of physical size of the simulated films) are done using the element size corresponding to the mesh with dimensions 16 x 14 x 1 for this $0.35\mu m$ thick film. This is a conservative choice as our experience indicates that gradients are largest in the thinnest case with most obstruction to plastic flow.

Next, we study the effect of number of grains on the stress-strain response of a passivated film with a thickness of $0.35\mu m$. The grain boundaries are considered to be impenetrable to plastic flow. The grains are oriented such that the misorientation between adjacent grains is 3-5 degrees about the x_3-axis (corresponding to orientation set 1). The response seems to be converging as

shown in Figure 4. Based on this observation, a film with 4 grains is used in all the simulations presented in this paper.

5. Results and Discussions

The effect of surface passivation, thickness and grain boundary constraints on the loading and unloading response of thin films is discussed in the following sub-sections.

5.1 Effect of Passivation

5.1.1 Loading: It is observed experimentally that the presence of a passivation layer makes the stress-strain response harder in comparison to unpassivated films (Xiang and Vlassak, 2006). In order to model this behavior, we begin with numerical experiments using conventional plasticity theory and orientation set 1 (mentioned in Section 4). Conventional plasticity may be recovered from *PMFDM* by setting $\boldsymbol{\alpha} = \boldsymbol{0}$ for all times and replacing (4) with

$$\boldsymbol{U}^e = grad\,\boldsymbol{u} - \boldsymbol{U}^p \;\; ; \dot{\boldsymbol{U}}^p = \boldsymbol{L}^p \;\; . \tag{30}$$

It is found that in conventional plasticity the stress-strain response is independent of the presence/absence of passivation layers (Figure 5). This is due to the absence of an explicit characterization of dislocations in the conventional plasticity framework. The same numerical experiment is now performed using *PMFDM*. Initially, grain boundaries are considered to be penetrable to dislocations. Figure 6(a) shows a significant difference in the stress-strain response between the passivated and the unpassivated films, with passivated films showing a harder response. This is due to the accumulation of polar dislocations along the passivation layer as shown in Figure 7(b). A thick layer of polar dislocations formed along the passivation layer acts as an obstruction to plastic flow. No such layer is formed in the case of unpassivated films as observed in Figure 7(d). The theory allows for greater hardening at material points with higher value of polar dislocation density and hence results in a harder response in the passivated films. An increase in hardening of the stress-strain response due to a passivation layer is also observed in numerical experiments that are performed using strain gradient plasticity

model (Xiang and Vlassak (2006)) and DD model (Nicola et al. (2006), Shishvan et al. (2010), Shishvan and Van der Giessen (2010)).

Next we consider the grain boundaries to be impenetrable to plastic flow. The stress-strain response still seems to get harder with passivation (Figure 6(b)). However, the difference in σ between the passivated and the unpassivated films is less in comparison to the unconstrained grain boundary case. The reason for this behavior is that constraints on plastic flow through grain boundaries result in the accumulation of polar dislocations along them as observed in Figure 7 (a), (c) and consequently decreases the relative effect of passivation layer on the stress-strain behavior.

All the results mentioned so far correspond to films with 3-5 degrees of misorientation between adjacent grains. In order to investigate the dependence of these results on grain orientation, similar computations as mentioned above are done for orientation set 2 and 3 (described in Section 4). Figure 8 shows the plot of σ at 1% applied strain for different cases. It is observed that the passivated films show a harder response than the unpassivated films for different sets of grain orientations. However, the value of σ at 1% applied strain changes significantly with the orientation, as expected.

5.1.2 Unloading/Bauschinger Effect: The main interest here is to analyze the Bauschinger effect during subsequent cycles of loading and unloading of multicrystalline thin films undergoing plane strain tension. It is observed experimentally that the passivated films show an unusual Bauschinger effect as compared to the films with no surface passivation (Xiang and Vlassak, 2006). The effect is not observed in the framework of conventional plasticity as shown in Figure 5. In *PMFDM*, the passivated films show a stronger Bauschinger effect than the unpassivated films due to the back stress associated with the accumulation of polar dislocations along the surface passivation layer (Figure 6(a), (b)).

The reverse plastic strain at the end of each unloading cycle is plotted against the pre-strain (at which unloading starts in every cycle) in Figure 9. Orientation set 1 with $h = 0.35\mu m$ is considered first. For the passivated film with penetrable grain boundaries,

the reverse plastic strain increases significantly on increasing the prestrain as observed in Figure 9(a). In the case of film with no passivation, zero reverse plastic strain is observed in the first cycle and relatively little in subsequent cycles. Similar trends are observed for impenetrable grain boundaries also. However, the difference in reverse plastic strain between the passivated and the unpassivated films is less in comparison to the unconstrained grain boundaries case (due to the reasons mentioned in Section 5.1.1).

On increasing the misorientation between adjacent grains from 3-5 degrees in orientation set 1 to 20-30 degrees (orientation set 2), the unpassivated films with penetrable grain boundaries show a non-zero reverse plastic strain (less in comparison to the passivated films) even in the first cycle (Figure 9(b)). This relatively little Bauschinger effect observed in the unpassivated films with unconstrained grain boundaries could be the result of dislocation accumulation along the grain boundaries (due to the misorientation between adjacent grains). Although the grain boundaries are penetrable, the misorientation between grains may cause some obstruction to the plastic flow. For the unpassivated film, a non-zero Bauschinger effect is observed in the case of orientation set 2 even in the context of classical plasticity, as shown in Figure 10. All other qualitative trends seem to be similar for different sets of grain orientation (Figure 9(b), (c)).

To better analyze the unloading behavior, two special cases are considered for orientation set 1 and $h = 0.35\mu m$. The mechanical response of films with (a) surface passivation and impenetrable grain boundaries, and (b) no passivation layer and penetrable grain boundaries, is compared on unloading at different strain levels instead of doing cycles of loading and unloading. It is evident from Figure 11(a) that the passivated film shows a very strong Bauschinger effect at all strain levels. Also, the plot of reverse plastic strain versus pre-strain is a straight line with zero slope in the beginning in the unpassivated film (Figure 11(b)).

5.2 Effect of Thickness (Size Effect)

5.2.1 Loading: In the plane strain bulge tests done by Xiang and Vlassak (2006), the passivated films show a very strong dependence of mechanical response on the thickness of films with thinner being stronger, whereas behavior of the unpassivated films is observed to be independent of the thickness. In order to model this behavior, two films with thicknesses of $h = 0.35\mu m$ and $h = 1.4\mu m$ are considered. This behavior cannot be modeled using conventional plasticity due to the absence of a length scale in the model (Figure 5).

Next, numerical experiments are performed using *PMFDM* to study the size effects in thin films. First, the grain boundaries are considered to be penetrable to dislocations. The passivated film with $h = 0.35\mu m$ shows a significantly harder response than the film with $h = 1.4\mu m$ (Figure 6(a)). In order to understand this behavior, the field plot of $|\boldsymbol{\alpha}|$ at 0.6% applied strain for the passivated films is shown in Figure 12 (a), (b). In this plot, the x_2 co-ordinate is scaled by the film thickness. It is evident from this figure that the thickness of dislocation layer along the surface passivation is more than double for the thin film in comparison to the thick film. The thickness of the dislocation layer (in scaled co-ordinates) decreases with an increase in the film thickness (the dependence of the scaled polar density layer width on the thickness of films is explained through dimensional analysis in Roy and Acharya (2006)). Clearly, the greater relative volume covered by this layer in the case of the thin film provides more work hardening as well as back stress representing microscopic internal stress effects not encapsulated in the internal stress field of $\boldsymbol{\alpha}$. In the case of unpassivated films, the response seems to be relatively independent of the thickness (Figure 6(a)), as observed in experiments.

In the case of impenetrable grain boundaries, the passivated films show a significant size effect with thinner being stronger (Figure 6(b)). However, a reverse size effect is observed in the case of unpassivated films (Figure 6(b)). This is due to the larger volume fraction of the body that is occupied by polar dislocations in the film with $h = 1.40\mu m$ in comparison to $h = 0.35\mu m$ as also discussed in Section 5.3.1.

Another observation is that the effect of thickness in the passivated films is more pronounced in the case of penetrable grain boundaries as compared to the impenetrable grain boundaries. Similar qualitative trends as mentioned above are observed for the different sets of grain orientations (Figure 13).

5.2.2 Unloading/Bauschinger Effect: It is observed in experiments that the magnitude of reverse plastic strain increases on decreasing the film thickness. This particular characteristic is initially analyzed for the orientation set 1. Classical plasticity shows similar unloading response for films of different thicknesses as shown in Figure 5. In the context of *PMFDM*, thinner *passivated* films show higher Bauschinger effect (Figure 9(a)). This thickness dependent unloading behavior could be due to the higher back stresses in thin films in comparison to the thick films. For the unpassivated films with penetrable grain boundaries, thickness has a very negligible effect on the unloading behavior, whereas in the case of constrained grain boundaries, the thicker films show a higher Bauschinger effect.

For the orientation set 2, it is found that the Bauschinger effect decreases with an increase in thickness in the passivated films whereas it seems to be independent of thickness for the unpassivated films. (Figure 9(b)).

For the orientation set 3, unloading behavior is independent of the film thickness in all the cases except for the passivated films with unconstrained grain boundaries. They show a reasonable size effect in unloading with thinner films having a higher magnitude of reverse plastic strain (Figure 9(c)). Thus, it can be concluded that the unloading behavior varies significantly with grain orientations.

5.3 Effect of Grain Boundary Constraints

5.3.1 Loading: The effect of constraints on plastic flow through grain boundaries on the mechanical behavior is discussed in this sub-section. Conventional crystal plasticity cannot be used to model the control of plastic flow through interfaces due to the absence

of an explicit characterization of dislocations in the model. Details of modeling in *PMFDM* are explained in Section 3.

First, a film with no surface passivation and $h = 0.35\mu m$ is considered. It is observed that the film with constrained grain boundaries shows a harder response as compared to the film with unconstrained grain boundaries, as shown in Figure 14(b). When the grain boundaries are impenetrable to dislocations, plastic flow is restricted which results in the accumulation of polar dislocations along the grain boundaries, as shown in Figure 7(c). The net polar dislocation density in the thin film is increased due to this obstruction and consequently results in a harder response. Similar behavior is observed in the unpassivated film with $h = 1.40\mu m$ as shown in Figure 14(d). It is important to note here that because the volume of the region of polar density accumulation is larger in the thicker film, the relative hardening between the grain-boundary-constrained and unconstrained case is greater than in the thinner unpassivated film.

In the film with surface passivation on both sides, the response is almost independent of the grain boundary constraints for $h = 0.35\mu m$ (Figure 14(a)). This is because the thickness of the layer of polar dislocations formed along the passivation layer is of the range of the film thickness as observed in Figure 7(a), (b). Thus, while constraining the grain boundaries does increase the volume of the body containing a higher polar dislocation density, as a whole this increase is not substantial. However, in the case of the thicker passivated film with $h = 1.4\mu m, \boldsymbol{\sigma} = \langle \boldsymbol{T}_{11} \rangle$ at 1% applied strain in the constrained grain boundary case is 1.1 times that of the film with unconstrained grain boundaries, according to expectation (Figure 14(c)).

Similar trends are observed in the case of orientation set 2 and 3 (Figure 15). However, the effect of grain boundary constraints on the stress strain behavior decreases on increasing the misorientation between adjacent grains from 3-5 degrees about x_3-axis in set 1 to 20-30 degrees in set 2. This is due to the fact that plastic flow through a grain

boundary decreases on increasing the misorientation between adjacent grains. Thus, a grain boundary with a higher misorientation acts as a naturally constrained boundary to the flow of dislocations and consequently not much difference is observed between the constrained and the unconstrained cases.

5.3.2 Unloading/Bauschinger Effect: The effect of constraints on plastic flow through grain boundaries on the unloading behavior is discussed in this sub-section. For the unpassivated films with grain orientations corresponding to set 1, the reverse plastic strain is higher in the films with impenetrable grain boundaries in comparison to the films with penetrable grain boundaries (Figure 9(a)). The effect is dominant in the films with $h = 1.4\mu m$ as compared to the films with $h = 0.35\mu m$. Bauschinger effect seems to be independent of grain boundary constraints in the case of passivated films.

In the case of orientation set 2, the response seems to be independent of the constraints on plastic flow through the grain boundaries irrespective of the film thickness and the presence/absence of passivation layer (Figure 9(b)).

In orientation set 3, similar trends as obtained for orientation set 1 are observed except that the Bauschinger effect in the *passivated* films with $h = 1.4\mu m$ seems to be sensitive to constraints on the plastic flow (Figure 9(c)).

5.4 Other Observations

It is observed from the set of numerical experiments performed in this paper that the effect of surface passivation layer on the mechanical response decreases with an increase in the thickness of films. This is shown more clearly in Figure 6(a) for the penetrable grain boundaries. The difference in $\sigma = \langle T_{11} \rangle$ between the passivated and the unpassivated films is higher for $h = 0.35\mu m$ as compared to that for $h = 1.40\mu m$. Similar behavior is observed in the case of impenetrable grain boundaries (Figure 6(b)).

5.5 Supplementary Remarks

5.5.1 In all the computations presented in this paper, the expression for $\boldsymbol{L}^p$ is used as mentioned in (11). However, these simulations were also done for following expression of $\boldsymbol{L}^p$ and are described in Puri (2009).

$$\boldsymbol{L}^p = \sum_{\kappa=1}^{n_{slip}} \dot{\gamma}^\kappa \boldsymbol{m}_0^\kappa \otimes \boldsymbol{n}_0^\kappa \tag{31}$$

Both expressions give similar results in terms of the stress-strain response for all cases presented in this paper. The motivation behind using (11) in this paper is an instability induced by (31) for very special grain orientations at large structural scales and in problems where homogeneous deformation is one solution[‡]. For most orientations we do not observe the instability. However, using the symmetric part of (31) as in (11) completely eliminates this instability. We believe that the origin of the instability may lie in the fact that in this small-deformation theory there is no 'feedback control,' through the driving force for $\boldsymbol{L}^p_{skw}$, on the growth of gradients in the skew part of $\boldsymbol{L}^p$. Ongoing work related to the finite deformation theory suggests that such control may arise naturally from theory.

5.5.2 Due to the use of a primarily explicit solution framework, constraint boundary conditions on $\boldsymbol{\alpha}\times\boldsymbol{V} + \boldsymbol{L}^p$ (plastic flow) cannot be accounted directly in the discretization of equations for $\boldsymbol{z}$. An auxiliary field $\boldsymbol{P}$ is introduced to implement the same boundary condition for plastic flow in solving for $\boldsymbol{z}$

$$\begin{aligned} &div\left(grad\ \dot{\boldsymbol{z}}\right) = div\left(\boldsymbol{P}\right) \\ &\boldsymbol{P} = \boldsymbol{\alpha}\times\boldsymbol{V} + \boldsymbol{L}^p \\ &\boldsymbol{P}\times\boldsymbol{n} = \left(\boldsymbol{\alpha}\times\boldsymbol{V} + \boldsymbol{L}^p\right)\times\boldsymbol{n}\ on\ \partial B \end{aligned} \tag{32}$$

However, we get almost similar results with and without the incorporation of this boundary condition in solving for $\boldsymbol{z}$ in different cases mentioned in this paper.

[‡] We are grateful to Justin Mach and Alan Needleman for discovering this instability and for associated discussions.

6. Conclusions

It is shown through numerical experiments that in the context of *PMFDM* theory, accumulation of polar dislocations along surface passivation layers result in a relatively (a) stiffer mechanical response, (b) thickness dependence of stress-strain response, and (c) significant Bauschinger effect in passivated films as compared to unpassivated films. Also, constraints on plastic flow through grain boundaries have a significant influence on size and Bauschinger effect. The results appear to be in good qualitative agreement with experimental observations (Xiang and Vlassak, 2006). However, the curvature of the stress-strain curves from experiments and simulations are different. This is a current shortcoming, much like the initial DD modeling for these experiments by Nicola et al. (2006), and needs to be rectified in the future. The resolution of this shortcoming may very well lie in better modeling of the effects of polar density on initial yield based on mechanisms of unambiguous physical origin, and this is a focus of our current research.

Acknowledgements: Support from the National Science Foundation (Grant Nos: DMI-0423304, DMR-0520425 CMU MRSEC), the US-ONR (Grant No. N000140910301), and the CMU Dowd-ICES Fellowship to SP is gratefully acknowledged.

References

- Acharya, A., 2001. A model of crystal plasticity based on the theory of continuously distributed dislocations. Journal of the Mechanics and Physics of Solids. 49, 761- 785.
- Acharya, A., 2003. Driving forces and boundary conditions in continuum dislocation mechanics. Proceedings of the Royal Society A. 459, 1343- 1363.
- Acharya, A., 2007. Jump condition for GND evolution as a constraint on slip transmission at grain boundaries. Philosophical Magazine. 87, 1349-1359.
- Acharya, A., 2011. Microcanonical Entropy and Mesoscale Dislocation Mechanics and Plasticity. Accepted in Journal of Elasticity.
- Acharya, A., Roy, A., 2006. Size effects and idealized dislocation microstructure at small scales: Predictions of a Phenonmenological model of Mesoscopic Field Dislocation Mechanics: Part I. Journal of the Mechanics and Physics of Solids. 54, 1687- 1710.

- Armstrong, P.J., and Frederick, C.O., 1966. A mathematical representation of the multiaxial Bauschinger effect. Technical Report C. E. G. B., Report RD/B/N731, Berkeley Nuclear Laboratories.
- Babic, M., 1997. Average balance equations for granular materials. Int. J. Eng. Sci. 35, 523-548.
- Bargmann, S., Ekh, M., Runesson, K., Svendson, B., 2010. Modeling of polycrystals with gradient crystal plasticity: A comparison of strategies. Philosophical Magazine. 90, 1263-1288.
- Ertürk, I., van Dommelen, J. A. W., Geers, M. G. D., 2009. Energetic dislocation interactions and thermodynamical aspects of strain gradient crystal plasticity theories. Journal of the Mechanics and Physics of Solids.57, 1801-1814.
- Espinosa, H.D., Prorok, B.C., and Peng, B., 2004. Plasticity size effects in free-standing submicron polycrystalline FCC -films subjected to pure tension. Journal of the Mechanics and Physics of Solids. 52, 667 – 689.
- Fleck, N.A., Hutchinson, J.W., 2001. A reformulation of strain gradient plasticity. Journal of the Mechanics and Physics of Solids. 49, 2245-2271.
- Gurtin, M.E., 2002. A gradient theory of single-crystal viscoplasticity that accounts for geometrically necessary dislocations. Journal of the Mechanics and Physics of Solids. 50, 5–32.
- Gurtin, M.E., Needleman, A., 2005. Boundary conditions in small-deformation, single-crystal plasticity that account for the Burgers vector. Journal of the Mechanics and Physics of Solids. 53, 1–13.
- Harder, J., 1999. A crystallographic model for the study of local deformation processes in polycrystals. International Journal of Plasticity. 15, 605-624.
- Kroner, E., 1981. Continuum theory of defects. In: Balian, R., et al. (Ed.), Physics of Defects, North-Holland Publishing Company, Amsterdam. 217–315.
- Kuroda, M., Tvergaard, V., 2008. On the formulations of higher-order strain gradient crystal plasticity. Journal of the Mechanics and Physics of Solids. 56, 1591-1608.
- Mach, J. C., Beaudoin, A. J., Acharya, A., 2010. Continuity in the plastic strain rate and its influence on texture evolution. Journal of the Mechanics and Physics of Solids. 58, 105-128.

- Mura, T., 1963. Continuous distribution of moving dislocations. Philosophical Magazine. 89, 843–857.
- Nicola, L., Xiang,Y., Vlassak, J.J., Van der Giessen, E. and Needleman, A., 2006. Plastic deformation of freestanding thin films: Experiments and modeling. Journal of the Mechanics and Physics of Solids. 54, 2089–2110.
- Nye, J. F., 1953. Some geometrical relations in dislocated crystals. Acta Metallurgica. 1, 153-162
- Puri S., 2009. Modeling dislocation sources and plastic flow through grain boundaries in mesoscopic field dislocation mechanics. Ph.D. Thesis.
- Puri, S., Roy, A., Acharya, A., Dimiduk, D., 2010. Modeling dislocation sources and size effects at initial yield in continuum plasticity, Journal of Mechanics of Materials and Structures. 4, 1603-1618.
- Roy, A., Acharya, A., 2005. Finite element approximation of field dislocation Mechanics. Journal of the Mechanics and Physics of Solids. 53, 143-170.
- Roy, A., Acharya, A., 2006. Size effects and idealized dislocation microstructure at small scales: Predictions of a Phenonmenological model of Mesoscopic Field Dislocation Mechanics: Part II. Journal of the Mechanics and Physics of Solids. 54, 1711- 1743.
- Shishvan, S. S., Nicola, L., Van der Giessen, E., 2010. Bauschinger effect in unpassivated freestanding thin films. Journal of Applied Physics. 107, 093529.
- Shishvan, S. S., Van der Giessen, E., 2010. Distribution of dislcoation source length and the size dependent yield strength in freestanding thin films. Journal of the Mechanics and Physics of Solids. 58, 678-695.
- Svendsen, B., Bargmann, S., 2010. On the continuum thermodynamic rate variational formulation of models for extended crystal plasticity at large deformation. Journal of the Mechanics and Physics of Solids. 58, 1253–1271.
- Taupin, V., Varadhan, S., Chevy, J., Fressengeas, C., Beaudoin, A. J., Montagnat, M., Duval, P., 2007. Effects of size on the dynamics of dislocations in ice single crystals. Phys. Rev. Lett. 99, 155507.
- Willis, J. R., 1967. Second-order effects of dislocations in anisotropic crystals. Int. J. Eng. Sci. 5, 171–190.

- Xiang, Y., Vlassak, J. J., 2006. Bauschinger and size effects in thin-film plasticity. Acta Materialia. 54, 5449-5460.

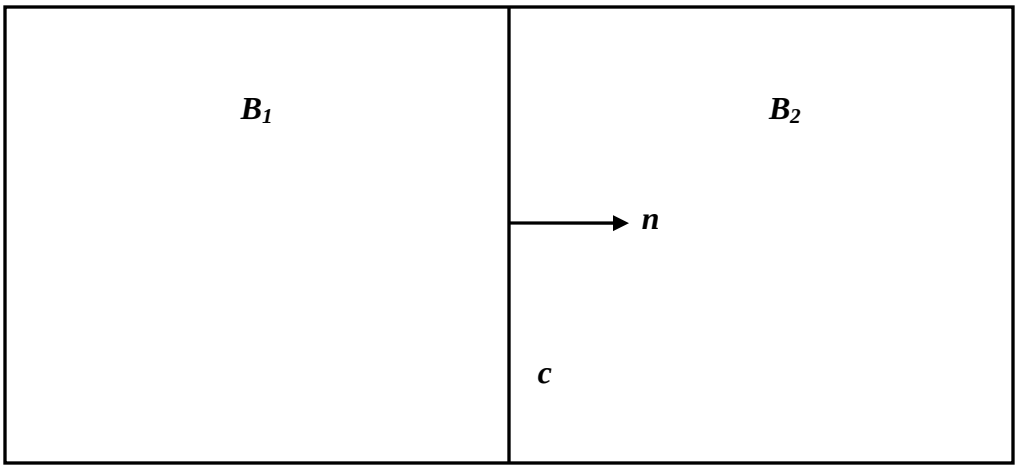

(a)

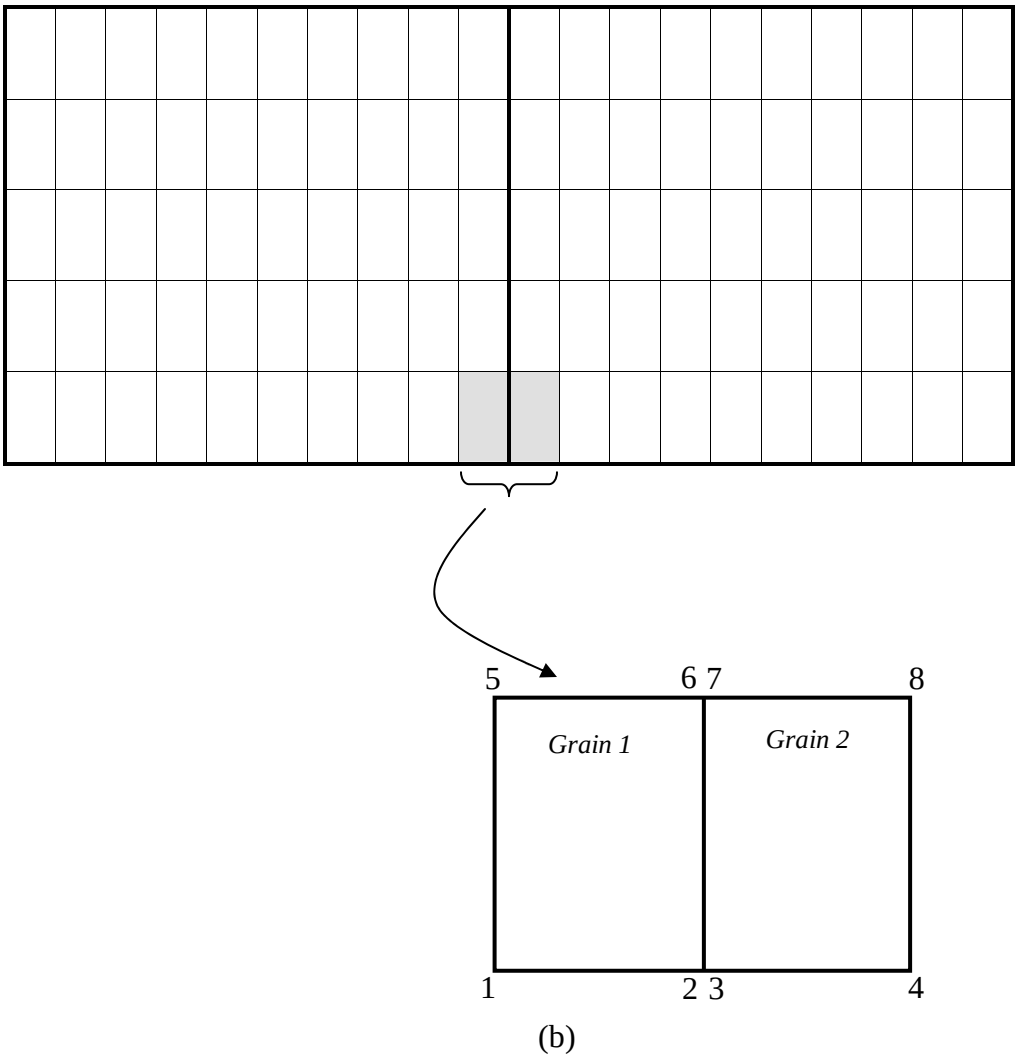

(b)

Figure 1. (a) Schematic of a bicrystal with grains, B_1 and B_2; (b) Node numbering of elements along the grain boundary.

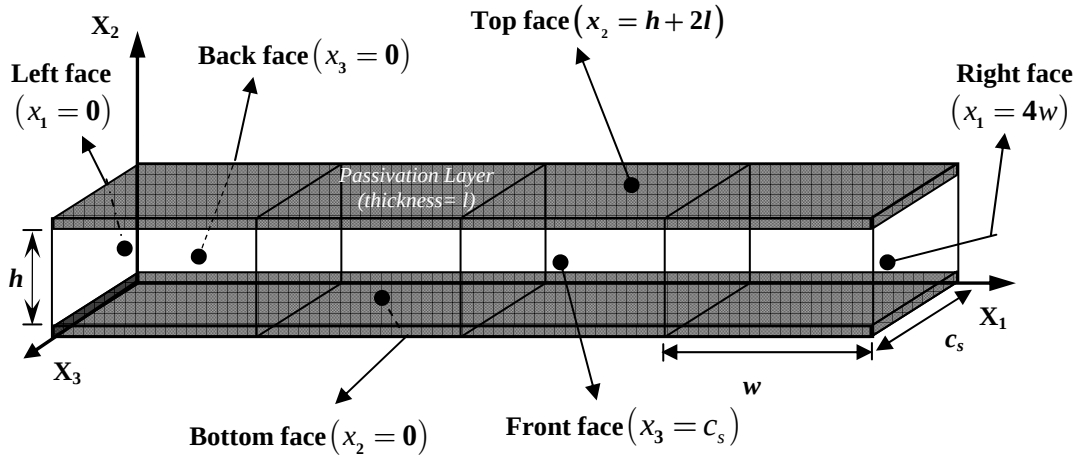

Figure 2. Schematic layout of typical model geometry (shaded portion represents the passivation layer)

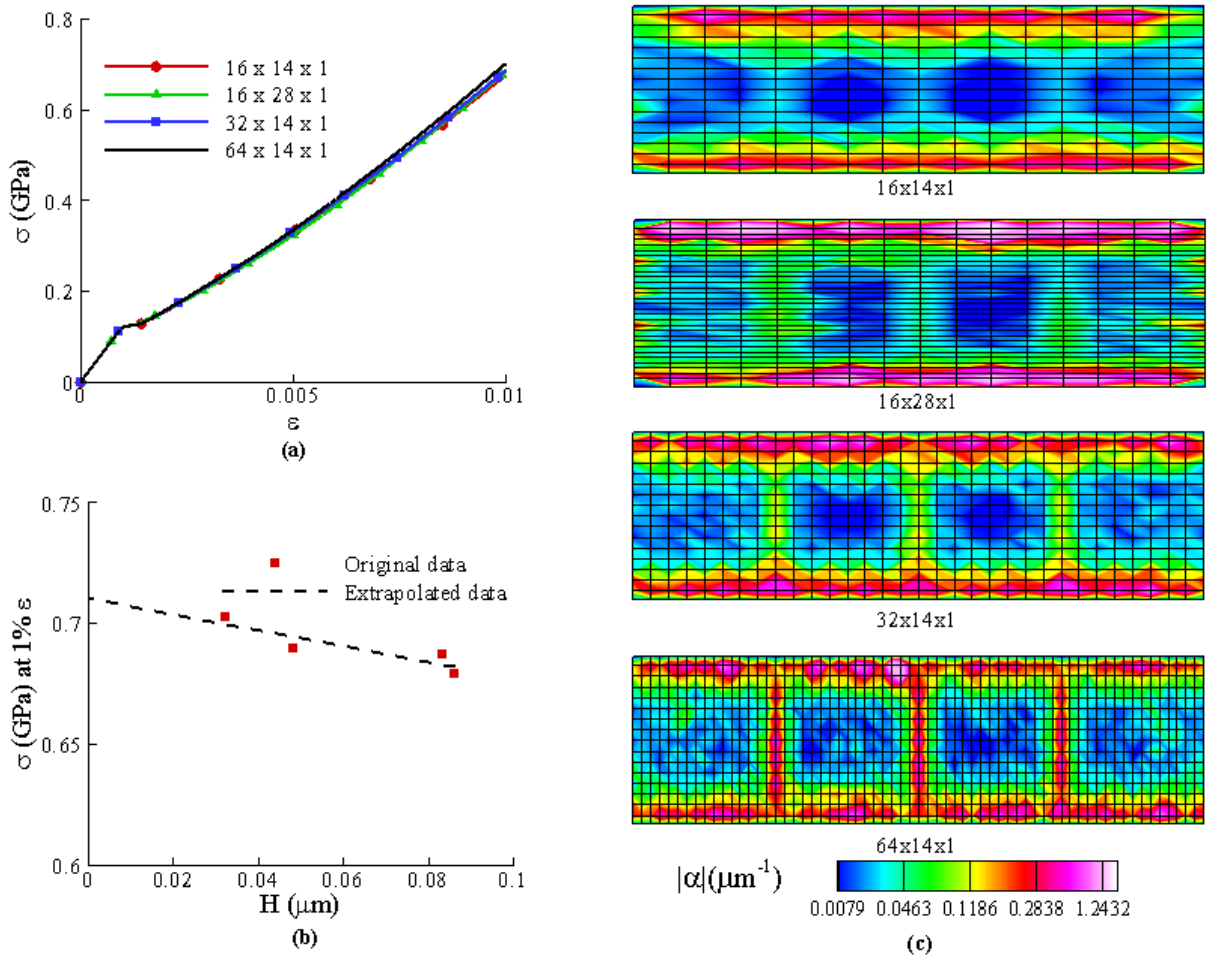

Figure 3. Convergence analysis for the film passivated on both sides and grain boundaries being impenetrable to dislocations ($h = 0.35\mu m$; orientation set 1); (a) stress-strain response for different element sizes; (b) σ at 1% applied strain plotted against the length of the diagonal (H) of an element (H is used as a representative measure of element size); (c) field plots of $|\alpha|$ at 0.6% applied strain for different element sizes.

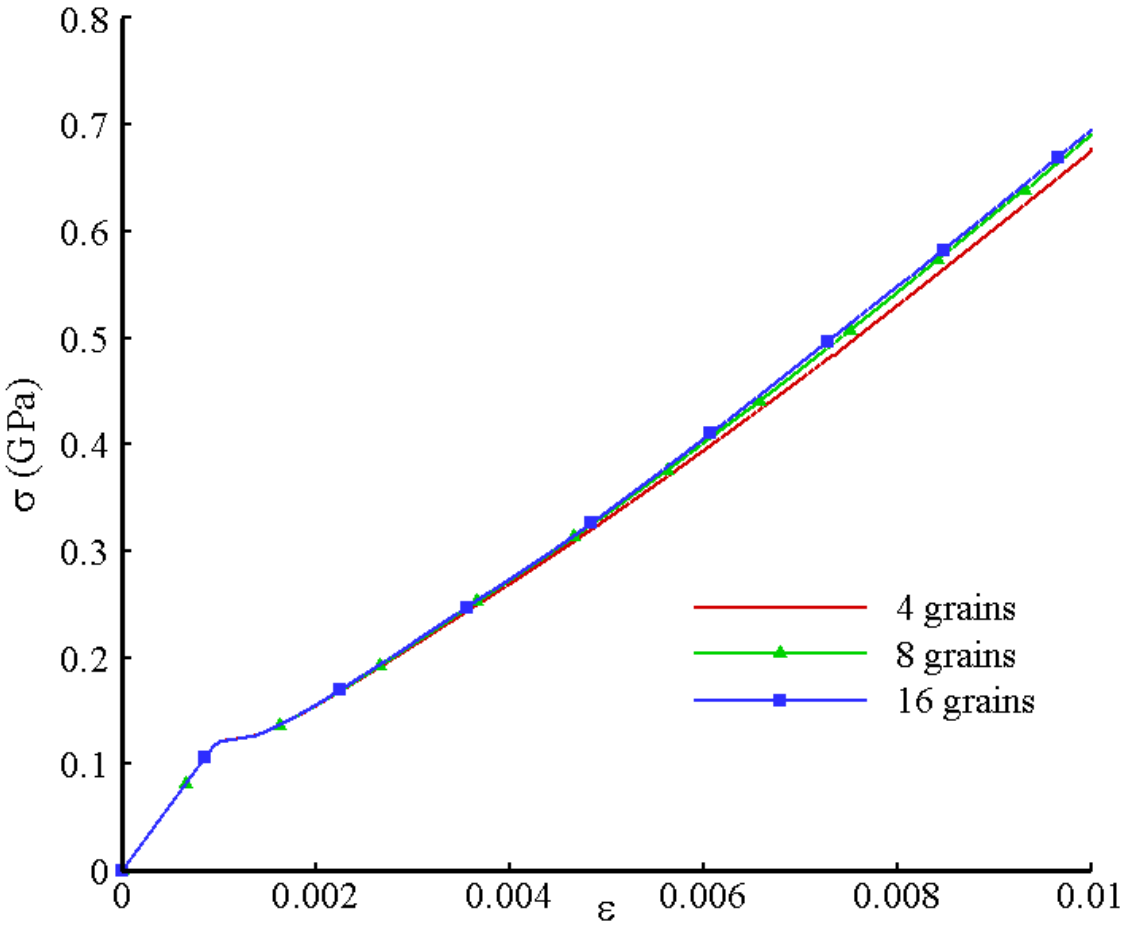

Figure 4. Convergence analysis with respect to number of grains for the film passivated on both sides and grain boundaries being impenetrable to dislocations ($h = 0.35 \mu m$; orientation set 1).

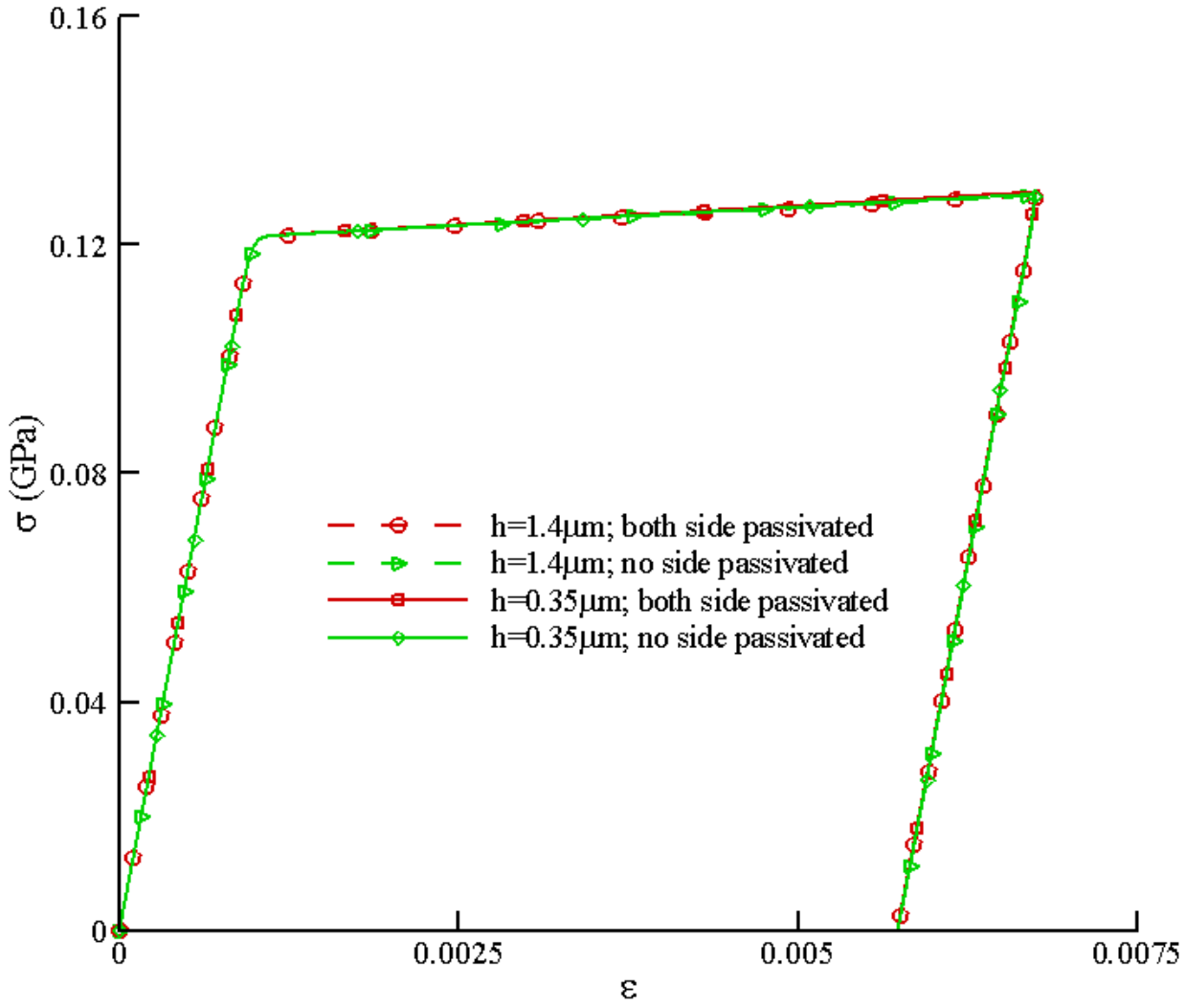

Figure 5. Stress-strain behavior of thin films using classical plasticity (orientation set 1).

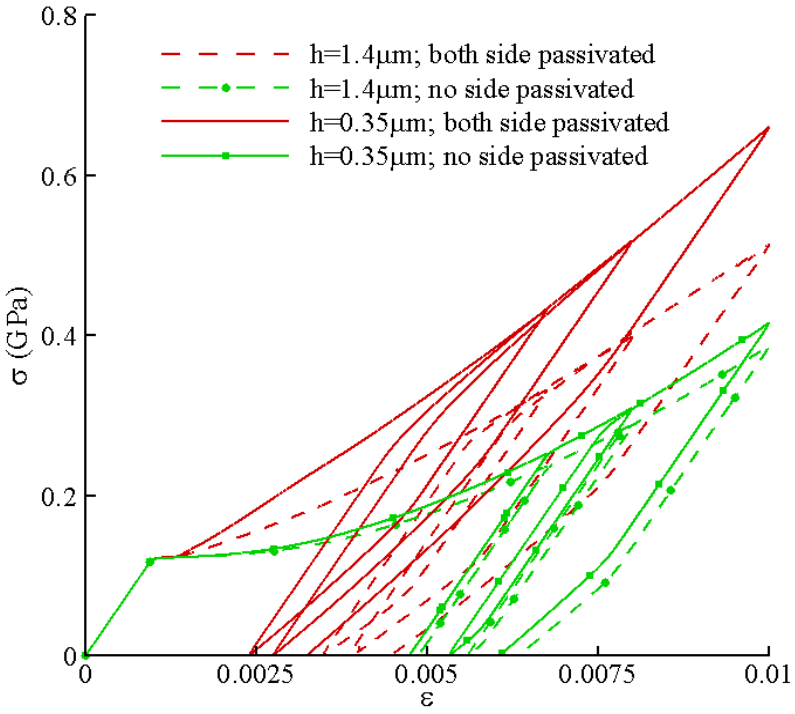

(a)

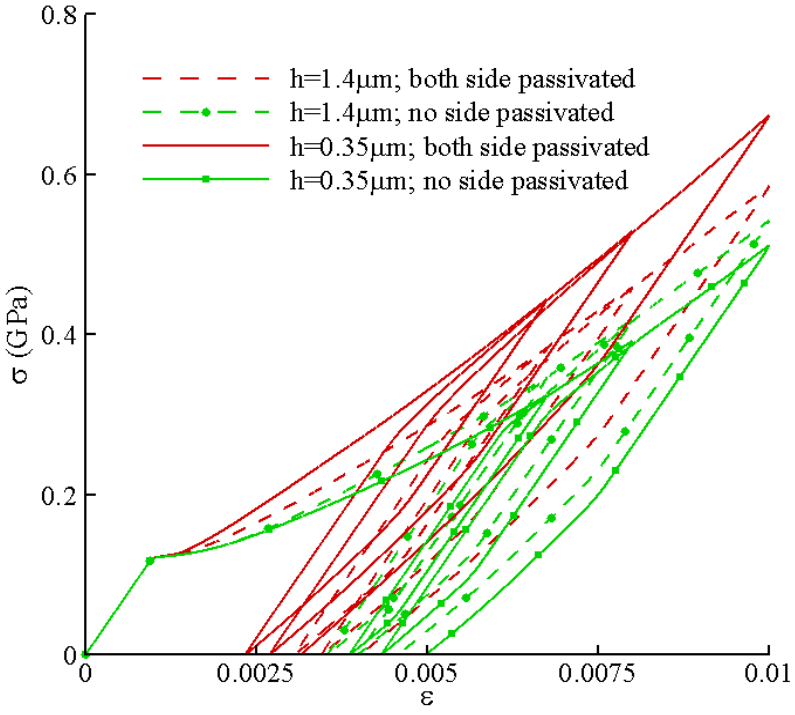

(b)

Figure 6. Stress-strain behavior of thin films undergoing cyclic loading using *PMFDM* (orientation set 1); (a) penetrable grain boundaries, (b) impenetrable grain boundaries.

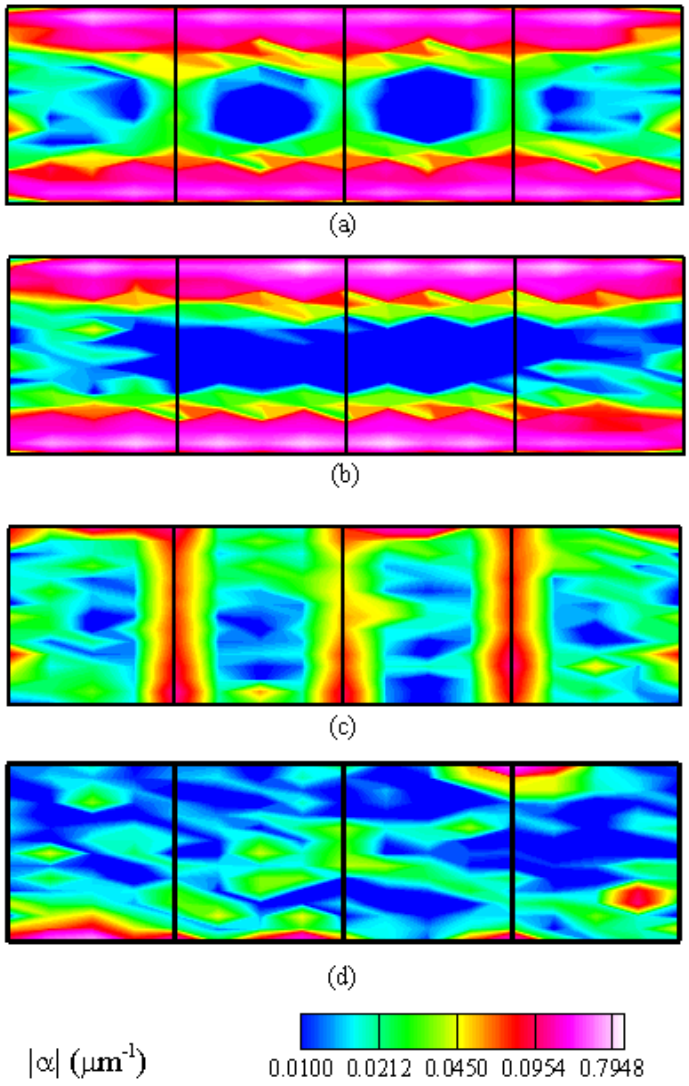

Figure 7. Field plot of $|\alpha|$ at 0.6% applied strain for $h = 0.35\mu m$ (orientation set 1) ; (a) both side passivated and constrained grain boundary, (b) both side passivated and unconstrained grain boundary, (c) no side passivated and constrained grain boundary, (d) no side passivated and unconstrained grain boundary.

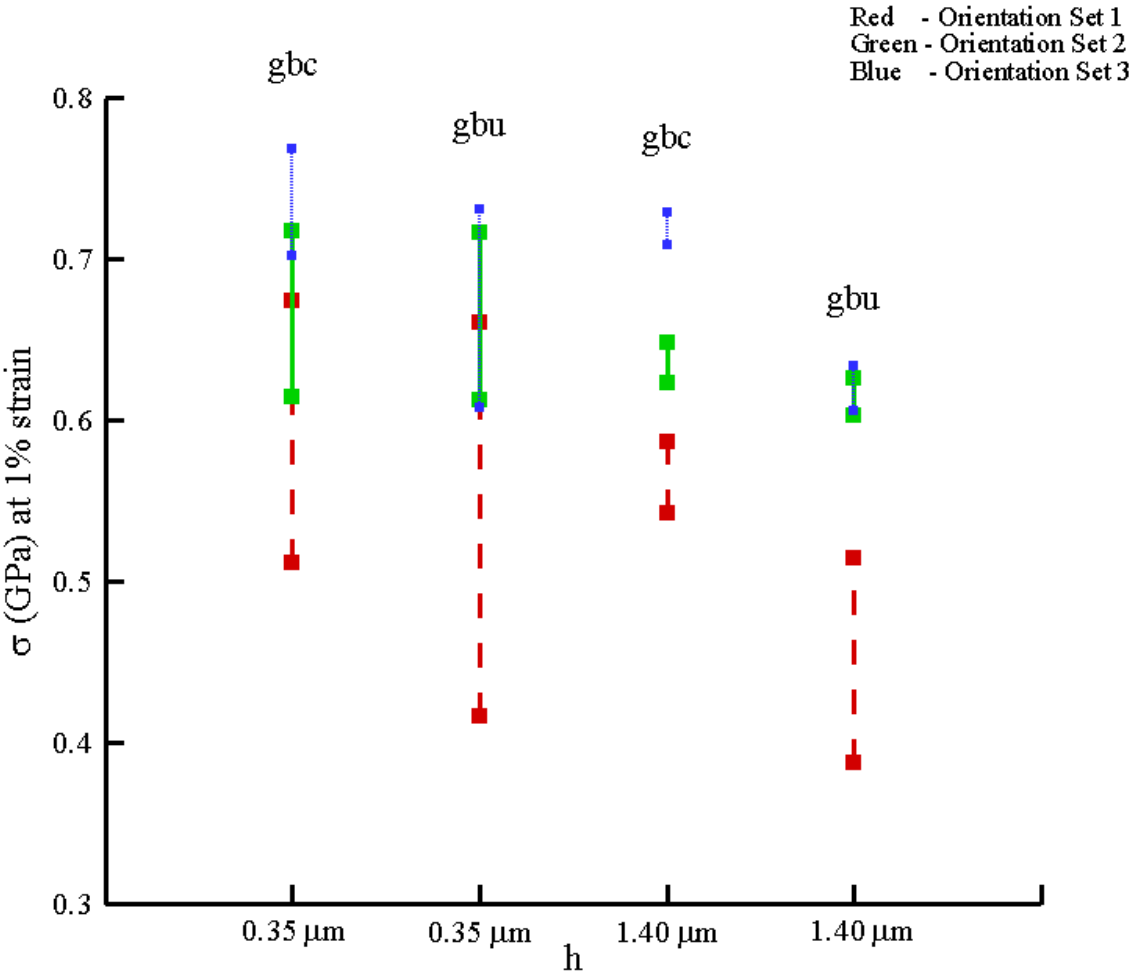

Figure 8. Effect of surface passivation on the stress-strain behavior of thin films for different orientation sets (For each line, bottom point represents unpassivated case and top point represents both side passivated case; ***gbc***- grain boundary constrained; ***gbu***- grain boundary unconstrained)

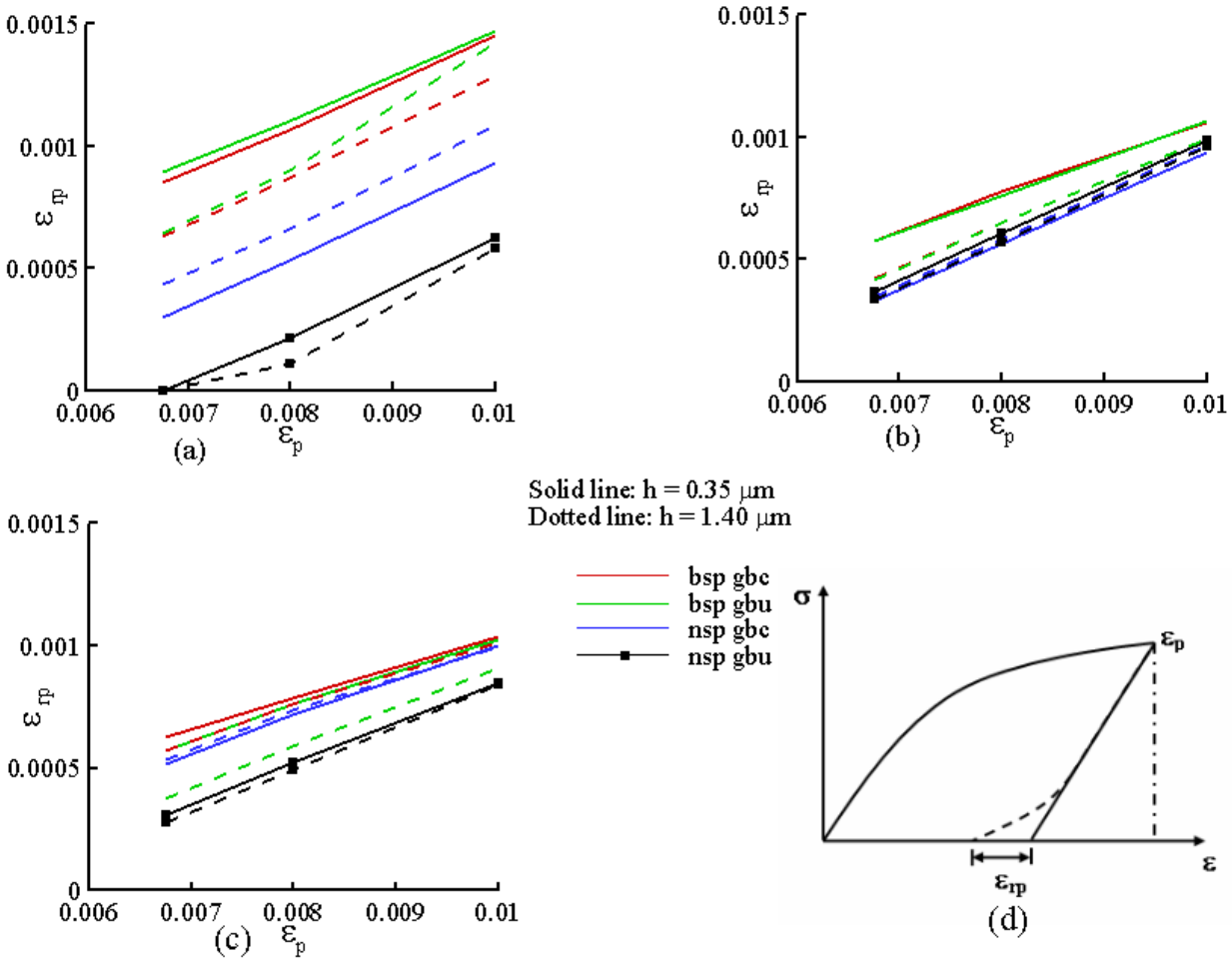

Figure 9. Effect of subsequent cycles of loading and unloading on Bauschinger effect; (a) Orientation set 1; (b) Orientation set 2; (c) Orientation set 3; (d) Schematic for defining reverse plastic strain (ε_{rp}) and pre-strain (ε_p) (after Xiang and Vlassak, 2006) (***bsp***- both side passivated; ***nsp***- no side passivated; ***gbc***- grain boundary constrained; ***gbu***- grain boundary unconstrained).

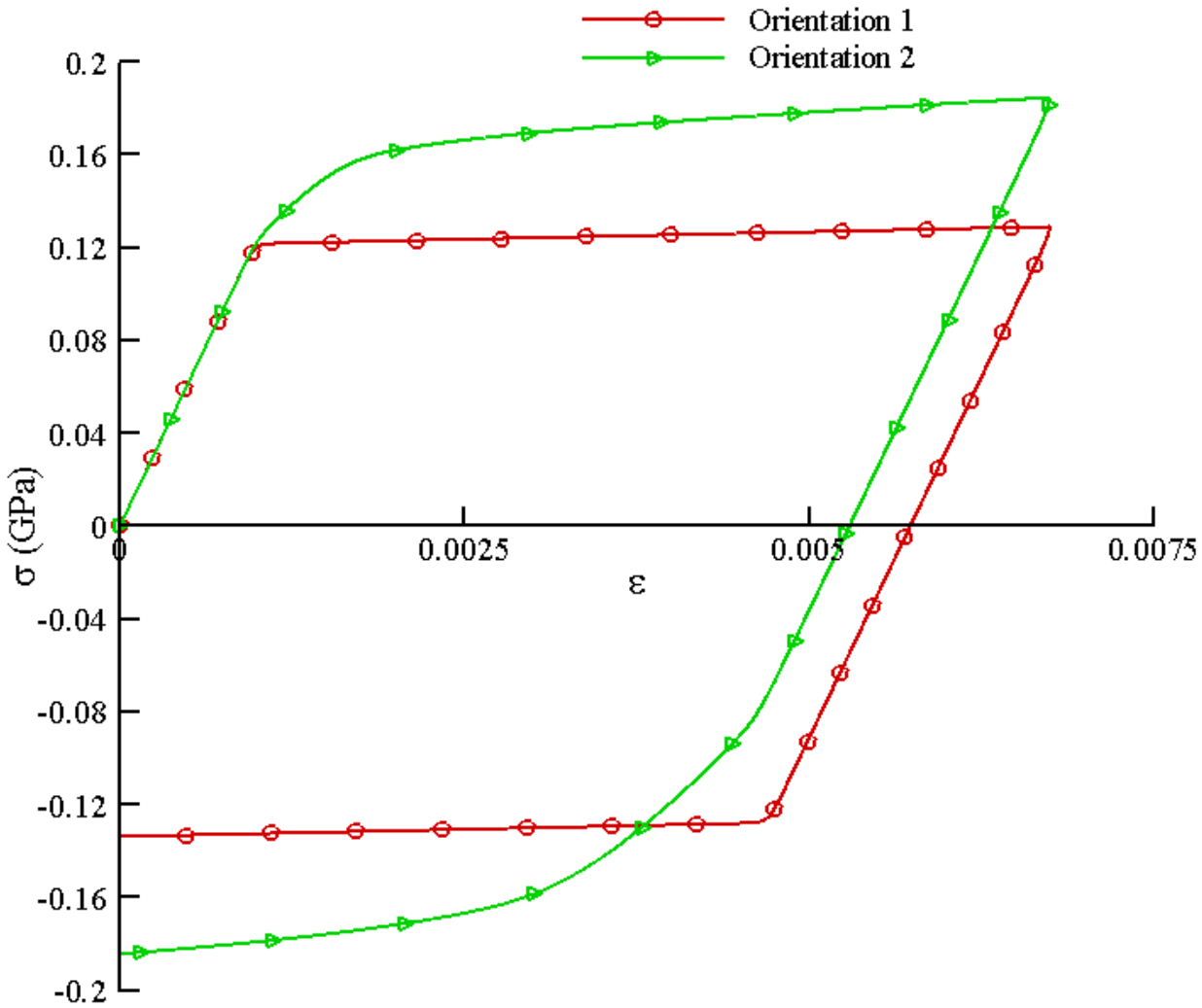

Figure 10. Comaprison of stress-strain response of thin films with grain orientations corresponding to set 1 and set 2 using classical plasticity.

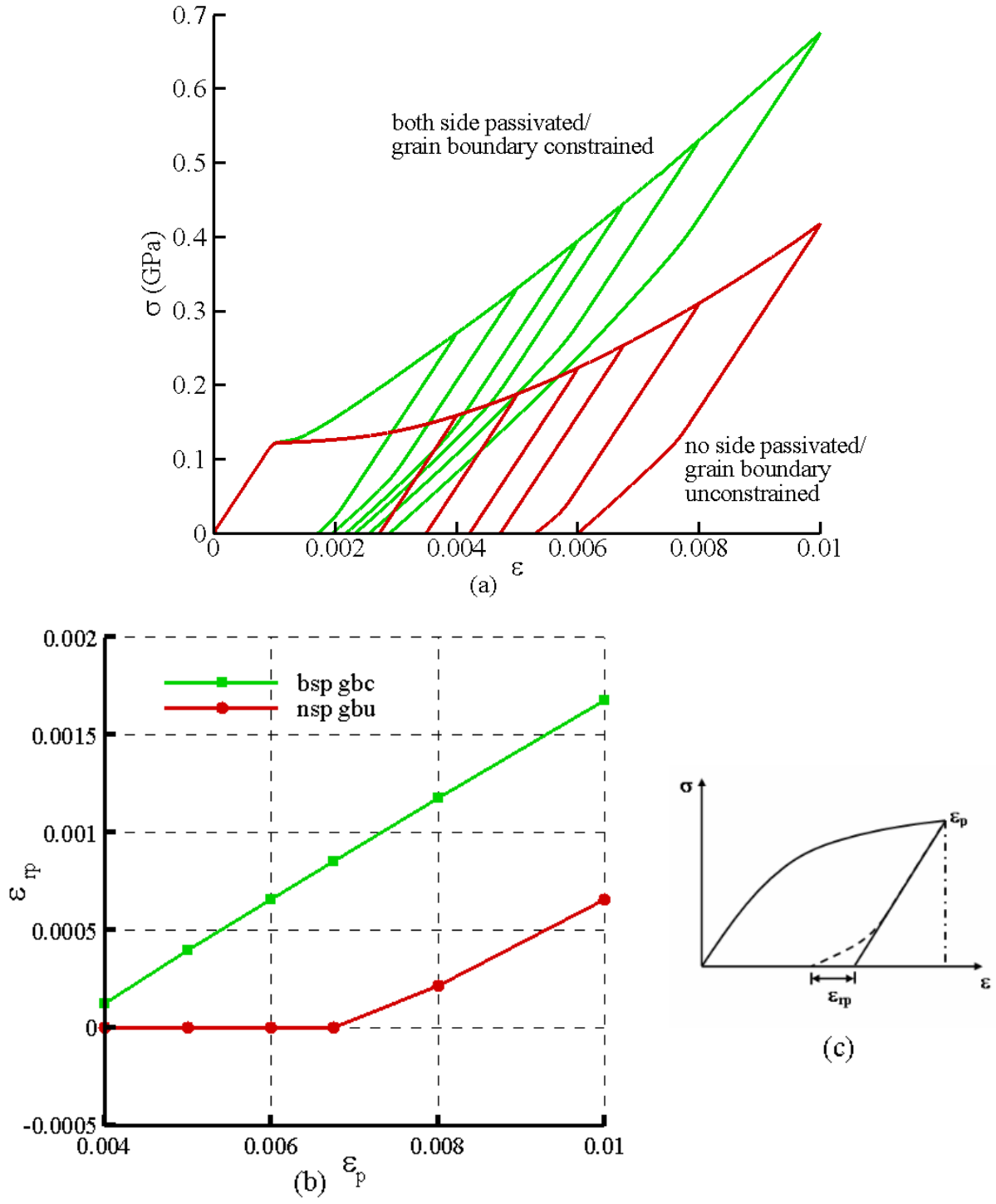

Figure 11. (a) Stress-strain behavior and (b) Bauschinger effect in thin films on unloading at different strain levels for $h = 0.35\mu m$; (c) Schematic for defining reverse plastic strain (ε_{rp}) and pre-strain (ε_p) (after Xiang and Vlassak, 2006) (***bsp***- both side passivated; ***nsp***- no side passivated; ***gbc***- grain boundary constrained; ***gbu***- grain boundary unconstrained).

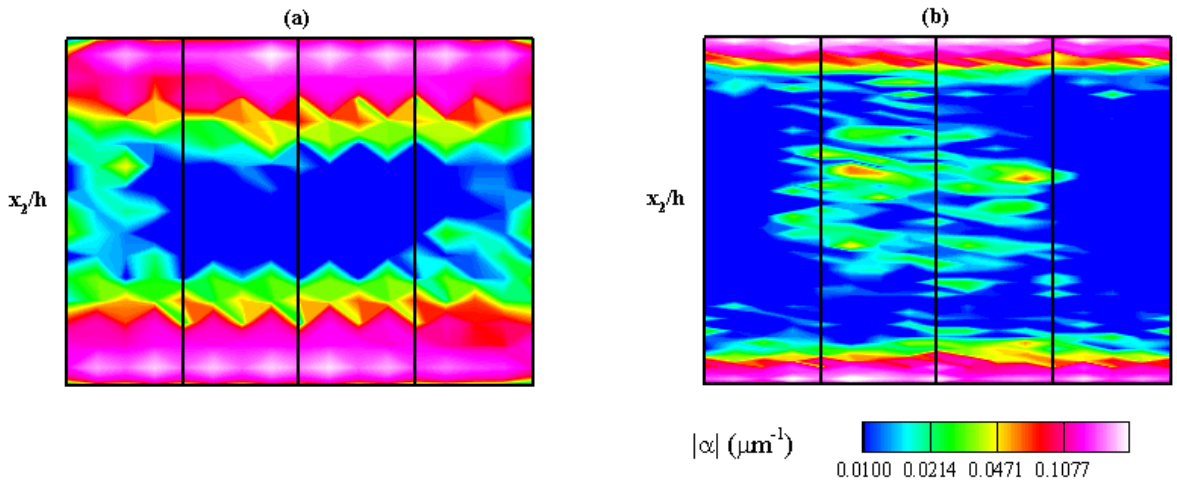

Figure 12. Field plot of $|\alpha|$ at 0.6% applied strain for both side passivated and unconstrained grain boundaries case; (a) $h = 0.35\mu m$ and (b) $h = 1.40\mu m$. X_2-coordinate in both films is normalized by their thickness.

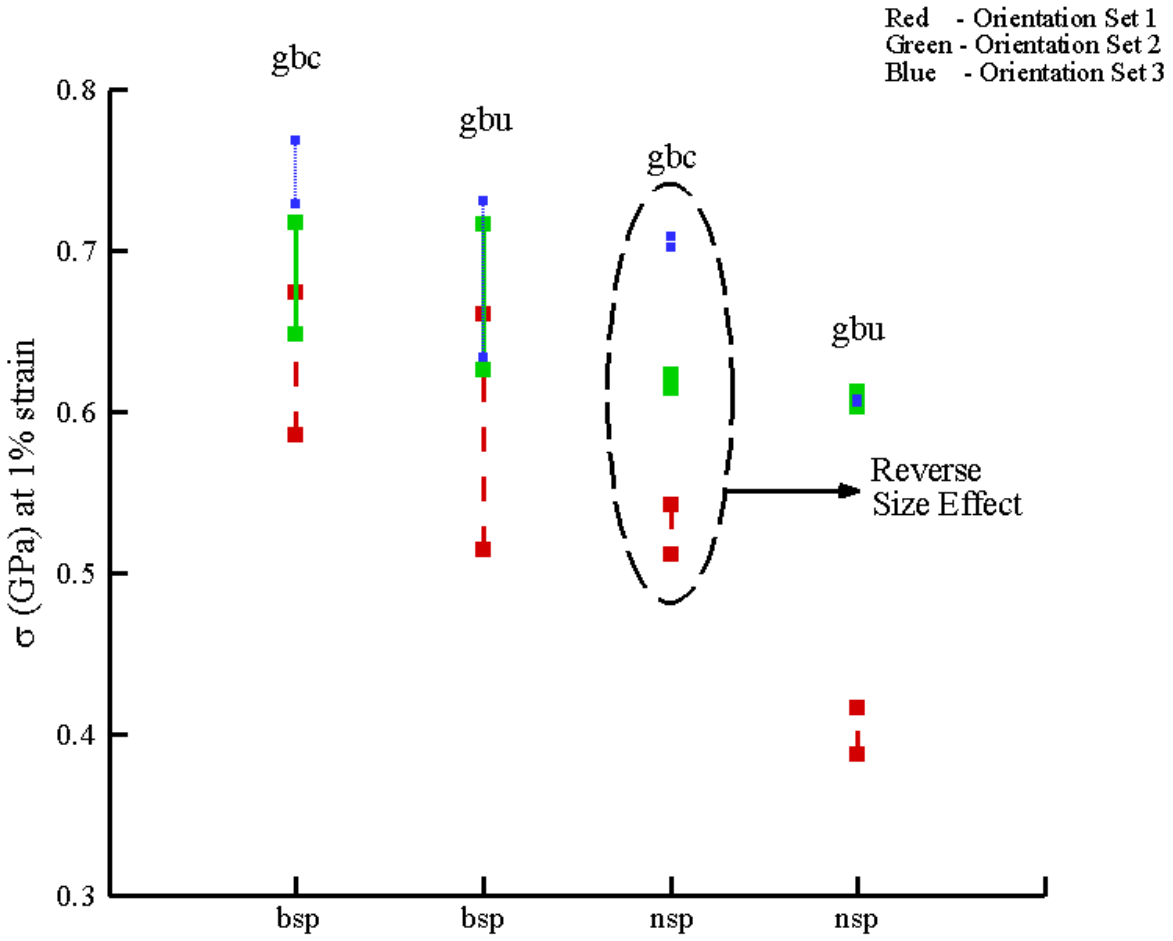

Figure 13. Effect of film thickness on the stress-strain behavior for different orientation sets (For each line, bottom point represents $h = 1.40\mu m$ and top point represents $h = 0.35\mu m$, except in no side passivated/grain boundary constrained case; ***bsp***- both side passivated*;* ***nsp***- no side passivated*;* ***gbc***- grain boundary constrained; ***gbu***- grain boundary unconstrained).

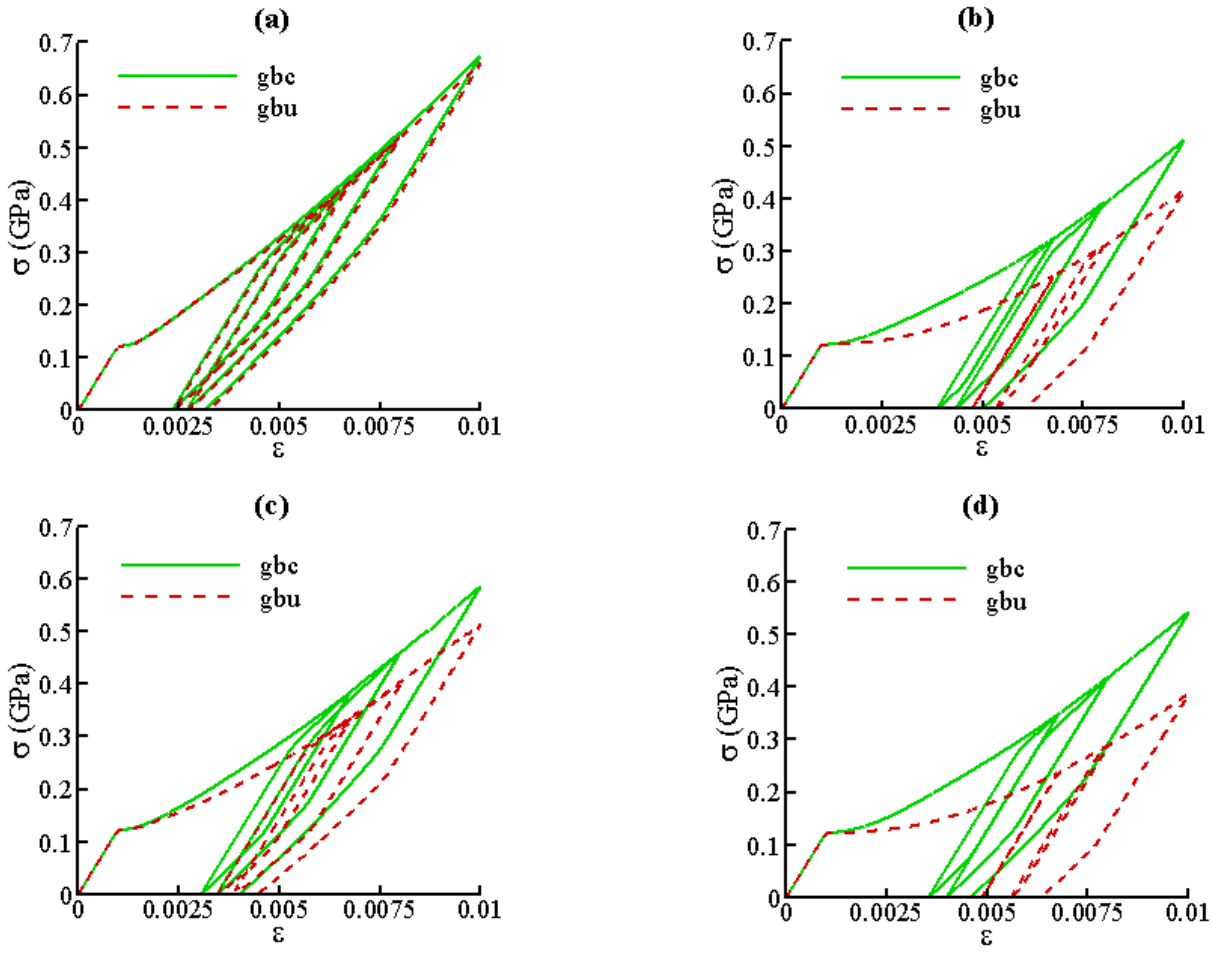

Figure 14. Effect of grain boundary constraints on the stress-strain behavior of films undergoing cyclic loading; (a) $h = 0.35\mu m$, both side passivated; (b) $h = 0.35\mu m$, no side passivated; (c) $h = 1.40\mu m$, both side passivated; (d) $h = 1.40\mu m$, no side passivated (***gbc***- grain boundary constrained; ***gbu***- grain boundary unconstrained).

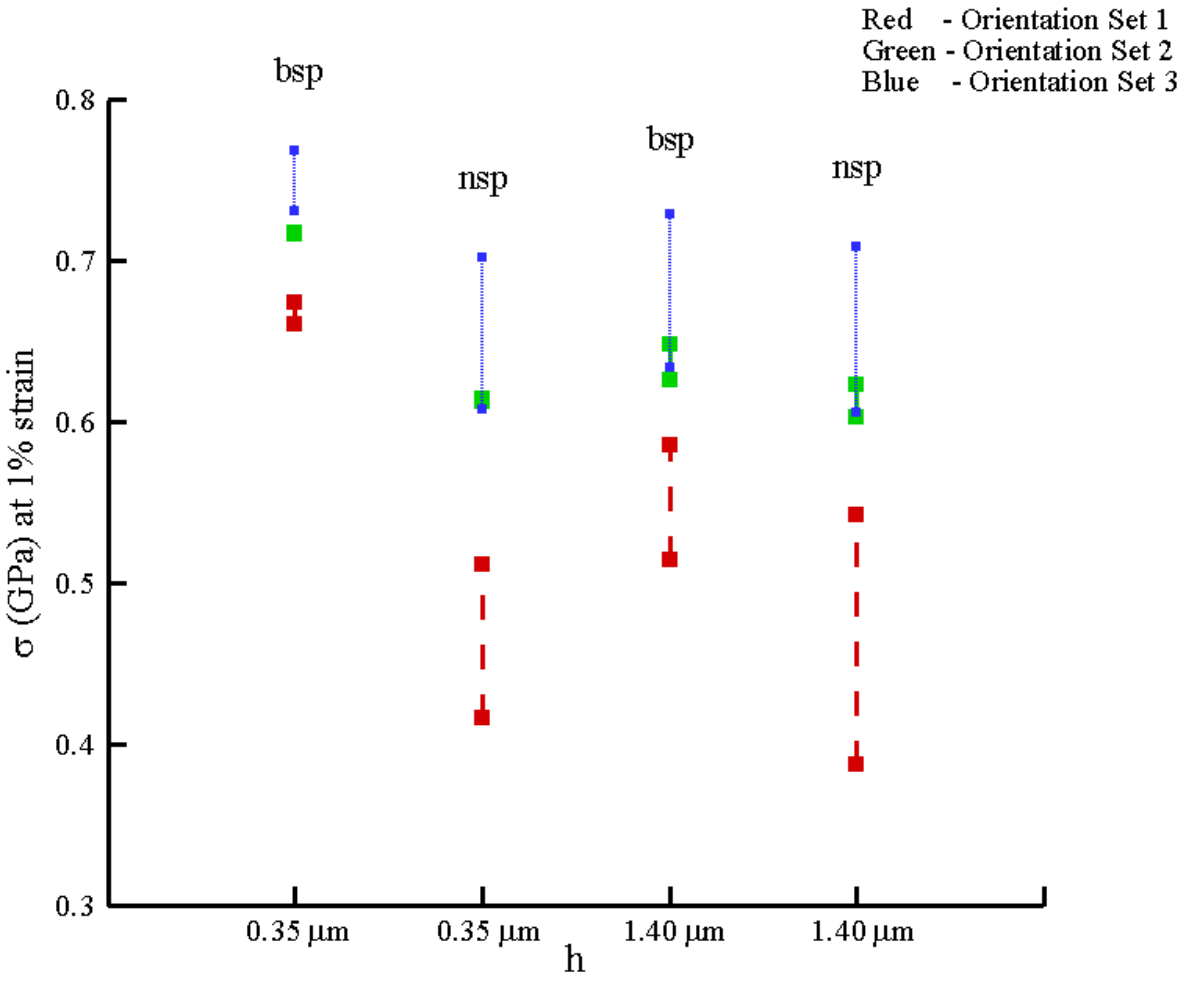

Figure 15. Effect of grain boundary constraints on the stress-strain behavior for different orientation sets (For each line, bottom point represents grain boundary unconstrained case and top point represents constrained case; ***bsp***- both side passivated; ***nsp***- no side passivated)